Reynolds Number Effects on a 5.2%-Scale High Lift Common Research Model

Sarah L. Langston *, Courtney S. Winski †, and Melissa B. Rivers ‡
NASA Langley Research Center, Hampton, VA, 23681, USA

A 5.2%-scale High Lift Common Research Model (CRM-HL) semispan wind tunnel model was tested at the National Transonic Facility (NTF) wind tunnel in Hampton, VA. One of the primary objectives of the NTF test was to determine the effect of varying Reynolds number on the configuration. The test used a combination of air and cryogenic nitrogen testing to obtain up to flight-like Reynolds numbers. The landing and takeoff configurations of the model were tested at speeds ranging from Mach 0.2 to 0.35. The Reynolds numbers based on the mean aerodynamic chord of the model ranged from 1.6 to 30 million. Overall, the lift increased with increasing Reynolds number for chord Reynolds numbers less than 16 million, following well-established trends. However, some anomalies in the force and moment data were observed in the linear region of the angle of attack range that did not follow expected trends. The force and moment results for both the landing and takeoff configurations are presented, along with surface pressure data for the landing configuration. Incremental effects from the landing gear, nacelle, and horizontal tail on the landing configuration are also presented.

Nomenclature

Symbols

α	=	Alpha / Angle of Attack, deg
BA_{CA}	=	Axial Coefficient Balance Accuracy
BA_{CN}	=	Normal Coefficient Balance Accuracy
BA_{CLM}	=	Pitching Moment Coefficient Balance Accuracy
C_{ref}	=	Wing Reference Chord
C_D	=	Drag Coefficient
C_L	=	Lift Coefficient
C_m	=	Pitching Moment Coefficient
C_p	=	Pressure Coefficient
M_∞	=	Freestream Mach Number
N_2	=	Nitrogen
S_{ref}	=	Semispan Wing Reference Area
q_∞ or Q	=	Dynamic Pressure, psf

Acronyms

BA	=	Balance Accuracy
CAD	=	Computer Aided Design
CFD	=	Computational Fluid Dynamics
CREYN	=	Chord Reynolds Number, Re_c
CRM	=	Common Research Model
CRM-HL	=	High Lift Common Research Model
IB	=	Inboard
IGV	=	Inlet Guide Vane
LaRC	=	Langley Research Center
LN_2	=	Liquid Nitrogen

*Research Aerospace Engineer, Configuration Aerodynamics Branch, AIAA Senior Member
†Research Aerospace Engineer, Configuration Aerodynamics Branch, AIAA Senior Member
‡Subproject Manager, Aeronautics Research Directorate, AIAA Associate Fellow

NASA	=	National Aeronautics and Space Administration
NTF	=	National Transonic Facility
OB	=	Outboard
TWICS	=	Transonic Wall Interference Correction System
NWB	=	Niedergeschwindigkeits-Windkanal Braunschweig
SMSS	=	Sidewall Model Support System
NR	=	Nacelle Radial
NC	=	Nacelle Chord
14x22	=	14- by 22-Foot Subsonic Tunnel

I. Introduction

The High Lift Common Research Model (CRM-HL) is a derivative of the high speed Common Research Model (CRM). In the late 2000s, the idea for a CRM was spurred by the need for open-source data that could be used for Computational Fluid Dynamics (CFD) validation and to increase the state-of-the-art in CFD and applied aerodynamics disciplines. The objective was to create a modern and relevant civil transport aircraft geometry suitable for applied CFD validation. The approach was to design a contemporary supercritical transonic wing and fuselage that is representative of a wide-body commercial transport aircraft. Key to the project was that the geometry would be open-source with publicly accessible data [1] and the design would allow for traditional and detailed flow measurements. The CRM design has since been tested in wind tunnels across the world with many international partners [2].

The CRM-HL derivative of the CRM was designed to address the need to explore the modeling and analysis of high-lift devices used in the landing and takeoff regimes of flight [3]. The objectives of the CRM-HL derivative are to:

- Generate high-quality wind tunnel data for use in CFD verification/validation studies;
- Improve and utilize advanced wind tunnel test and measurement techniques;
- Support research activities in low-speed aerodynamic design, performance enhancement, noise reduction, and / or high-lift system simplification.

The 5.2%-scale CRM-HL wind tunnel model [4] is one of the NASA contributions to the CRM-HL ecosystem. The NASA 5.2%-scale semispan model has been tested at the 14- by 22-Foot Subsonic Tunnel (14x22) [5], located at the NASA Langley Research Center (LaRC) in Hampton, VA and the Niedergeschwindigkeits-Windkanal Braunschweig (NWB) wind tunnel in Braunschweig, Germany [6].

The focus of this paper is the Reynolds number effects on the forces and moments of the NASA 5.2%-scale semispan model in the National Transonic Facility (NTF) conducted in late 2023 and early 2024, where the landing configuration was the primary configuration of focus.

II. Wind Tunnel Facility

The NTF, located at LaRC, is the world's largest fan-driven, closed-circuit, continuous-flow, pressurized cryogenic transonic wind tunnel [7, 8]. The NTF can operate in air, nitrogen, or mixed mode to obtain Reynolds numbers near or at flight conditions by varying Mach number, temperature, and pressure independently. The NTF has a Mach number range of 0.2 to 1.2, a temperature range of 120°F (air) to -250°F (nitrogen), and an absolute pressurization range of 15 to 125 pounds per square inch (PSIA).

The NTF has an 8.2-foot square test section that is 25 feet long. The test section ceiling and floor are slotted and held at 6% open. The side walls are solid. Figure 1 is a schematic of the tunnel circuit with key components highlighted. Of note are the inlet guide vanes (IGV) shown in the upper right of the figure, which allow for fine Mach control and the liquid nitrogen (LN_2) injectors shown in the lower right of the figure, which inject liquid nitrogen into the flow, which is then vaporized to obtain the low temperatures necessary for cryogenic testing. The fan blades can be seen behind the IGVs in the upper right of Figure 1. The test section can support full-span sting mounted models as depicted in Figure 1 or a side-wall balance can be used to support semispan models. The facility envelope of unit Reynolds number and Mach number in the air, nitrogen (N_2), and mixed mode of operations is depicted in Figure 2.

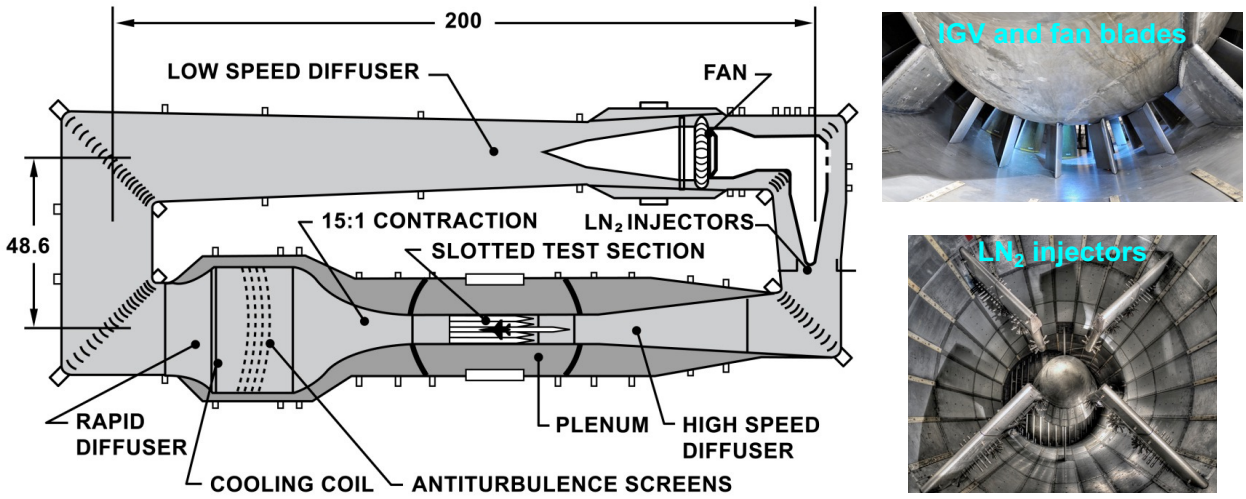


Fig. 1 Schematic of the NTF wind tunnel circuit with key components labeled (all linear dimensions are in feet) [Photos: NASA].

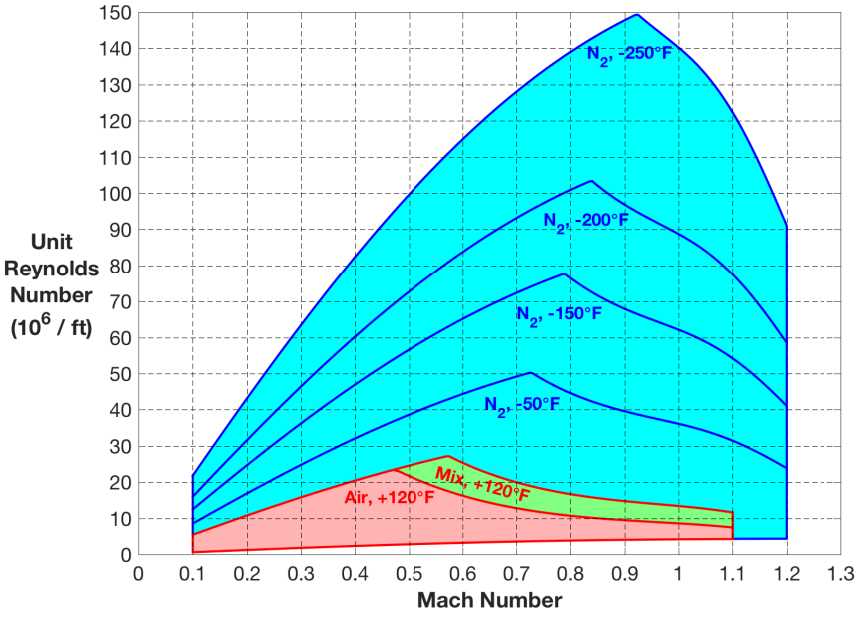


Fig. 2 NTF operation ranges for unit Reynolds number as a function of Mach number.

III. Wind Tunnel Model Description

The NASA 5.2%-scale semispan model was designed at LaRC, and followed the outer model line definitions for the CRM-HL as defined in Refs. [3] and [9]. The geometry files for the CRM-HL can be found on the CRM website [1]. The model was designed to be modular with the ability to modify the slat angle, inboard and outboard flap angles independently, as well as test with nacelle, landing gear, and horizontal tail on and off. The model used a newly manufactured wing that mounted to an existing 5.2%-scale fuselage that had been used for prior testing at the NTF. Only minor modifications to the fuselage cover plates were necessary. The model reference sizes are shown in Table 1.

Table 1 Full-scale and 5.2%-scale model reference dimensions.

Parameter	Full-Scale	5.2%-Model Scale
Semispan Wingspan	1156.75 inches	60.15 inches
Reference Chord (C_{ref})	275.8 inches	14.34 inches
Semispan Reference Area (S_{ref})	2065 square feet	5.58 square feet
Fuselage Length	205.96 feet	10.71 feet

The model was primarily manufactured from Vascomax™, which will maintain structural integrity and performance over the large temperature range (+120°F to -250°F) that the model will experience during testing in the NTF. A Computer Aided Design (CAD) rendering of the main wing assembly with key components labeled is shown in Figure 3. The specific deployed slat and flap angles for the takeoff and landing configurations are listed in Table 2. Both the slat and the flap angles are set using specifically angled brackets, with the deployed slat or flap parts remaining the same and only the brackets changing to alter the angle. CAD renderings of the slat and flap brackets are shown in Figures 4 and 5, respectively. The nacelle included a chine installed in the middle position, as show in Figure 3, for the entirety of the test. The nacelle and portions of the landing gear were additively manufactured out of Inconel, and the rest of the model was traditionally manufactured.

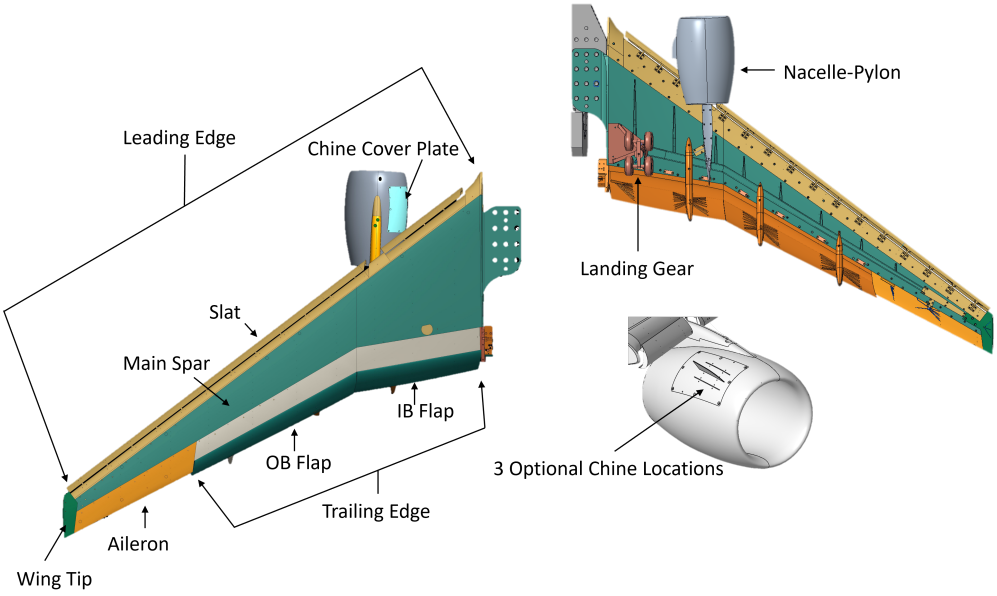


Fig. 3 CAD rendering of the main wing assembly with key components labeled.

Table 2 Slat and flap angles for the takeoff and landing configurations.

Flight Configuration	Slat	Inboard (IB) Flap	Outboard (OB) Flap
Takeoff	22 degrees	25 degrees	25 degrees
Landing	30 degrees	40 degrees	37 degrees

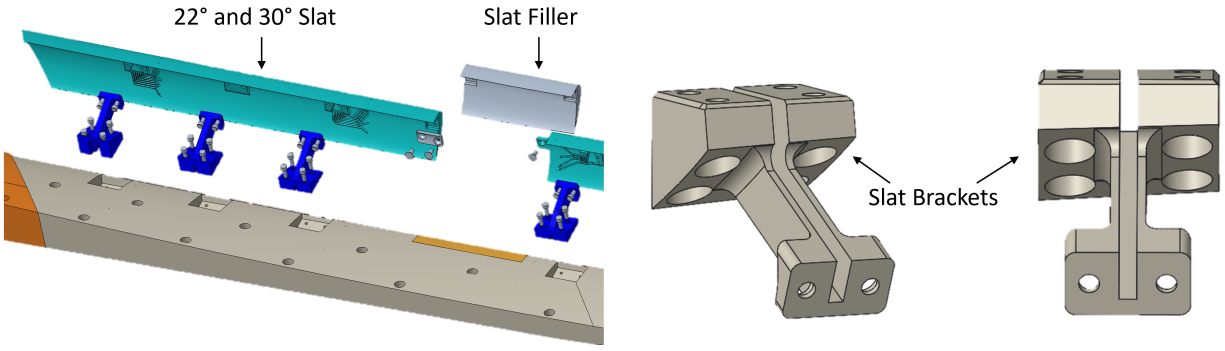


Fig. 4 CAD rendering of slat assembly with a highlight of the slat brackets used to set the deployed slat angle.

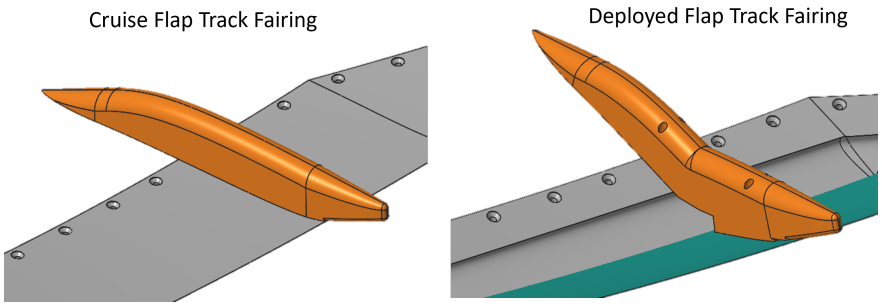


Fig. 5 CAD rendering of flap bracket assembly.

The primary data collected during the 5.2%-scale CRM-HL NTF test were forces, moments, and surface pressures. Other measurements, including model deformation and flow visualization data, will be the focus of future publications. The force and moment data were acquired using an external balance, NTF-117S [10]. Balance accuracy (BA) and calibration loads are shown in Table 3. One sigma balance accuracy of the force and moment coefficients at the dynamic pressures tested are shown in Table 4. The equation to calculate the force coefficient balance accuracy is shown in Equation 1 and the equation to calculate the pitching moment coefficient balance accuracy is shown in Equation 2.

$$BA_{ForceCoefficient} = \frac{BA_{Force}}{Q * S_{ref}} \tag{1}$$

$$BA_{PitchingMomentCoefficient} = \frac{BA_{PitchingMoment}}{Q * S_{ref} * C_{ref}} \tag{2}$$

The NTF-117S is located within the Sidewall Model Support System (SMSS), which is mounted through the far side wall of the NTF test section. As the model is wall mounted, the wing is tested in a horizontal position. A diagram of the model connection to the balance is shown in Figure 6 and the CRM-HL installed in the NTF test section is shown in Figure 7. The model installation includes a standoff that has been sized from previous testing and analysis of the existing fuselage that should preclude any effects of the sidewall boundary layer on the model.

Table 3 Calibration loads and accuracy for the NTF 117S balance.

Component	Full Scale Calibration	% Full Scale Accuracy (95% conf)	Effective Balance Accuracy (BA)
Normal Force	±12,000 lb	0.05	6 lb
Axial Force	±1,800 lb	0.14	2.25 lb
Pitching Moment	±90,000 in-lbf	0.16	144 in-lbf
Rolling Moment	±669,000 in-lbf	0.12	802.8 in-lbf
Yawing Moment	±100,350 in-lbf	0.09	90.3 in-lbf
Side Force	-	-	-

Table 4 NTF-117S one sigma balance accuracy of the force and pitching moment coefficients at dynamic pressures tested.

Q (psf)	BA_{CN}	BA_{CA}	BA_{CLM}
61	0.0176	0.0074	0.0295
82	0.0131	0.0055	0.0219
101	0.0106	0.0045	0.0178
133	0.0081	0.0034	0.0135
138	0.0078	0.0033	0.013
157	0.0068	0.0029	0.0115
207	0.0052	0.0022	0.0087
210	0.0051	0.0022	0.0086
240	0.0045	0.0019	0.0075
295	0.0036	0.0015	0.0061

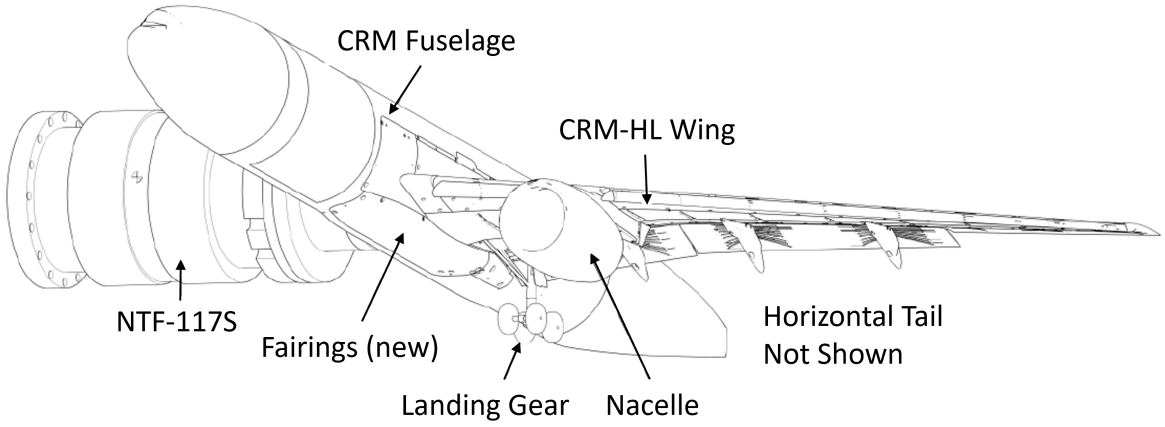


Fig. 6 Diagram of balance connection to 5.2%-scale CRM-HL.



Fig. 7 The 5.2%-scale CRM-HL installed in the NTF test section [Photo: NASA].

The 5.2%-scale CRM-HL model is instrumented with static pressure ports distributed throughout the main element, aileron, leading and trailing edges [(for cruise and deployed configurations) flaps and slats] and nacelle. The number of static pressure ports recorded was configuration dependent, as not all model parts were installed at the same time. For example, only either the deployed trailing edge with flaps or the cruise trailing edge could be installed at any one time. This led to a different number of static pressure ports connected between each of the landing, takeoff, and cruise configurations. The maximum number of static pressure ports on the model was 309, corresponding to the deployed configurations with the nacelle on. The wing static pressure ports were distributed on the upper and lower surface at ten different wing stations across the span. The pressure ports were perpendicular to the highlight of the leading edge and angled to the streamwise direction ahead of the 25% local wing chord. Behind the 25% local wing chord location the pressure ports followed the wing chord lines [4, 6]. The number of wing pressure ports varied between 292 (deployed leading and trailing edges with slat and flaps) and 188 (cruise leading and trailing edges). The locations of the 10 spanwise stations for the pressure ports on the wing are shown in Figure 8, where the color coding corresponds to their part location (i.e., main element, flap, or slat). The nacelle was also instrumented with 17 static pressure ports; the locations are shown in Figure 9. In the figure, the ports are identified as Nacelle Chord (NC) and Nacelle Radial (NR) depending on the location of the port. Additional static pressure data were collected on the fuselage and the model was instrumented with 16 unsteady pressure transducers, but those results will not be referenced in this paper.

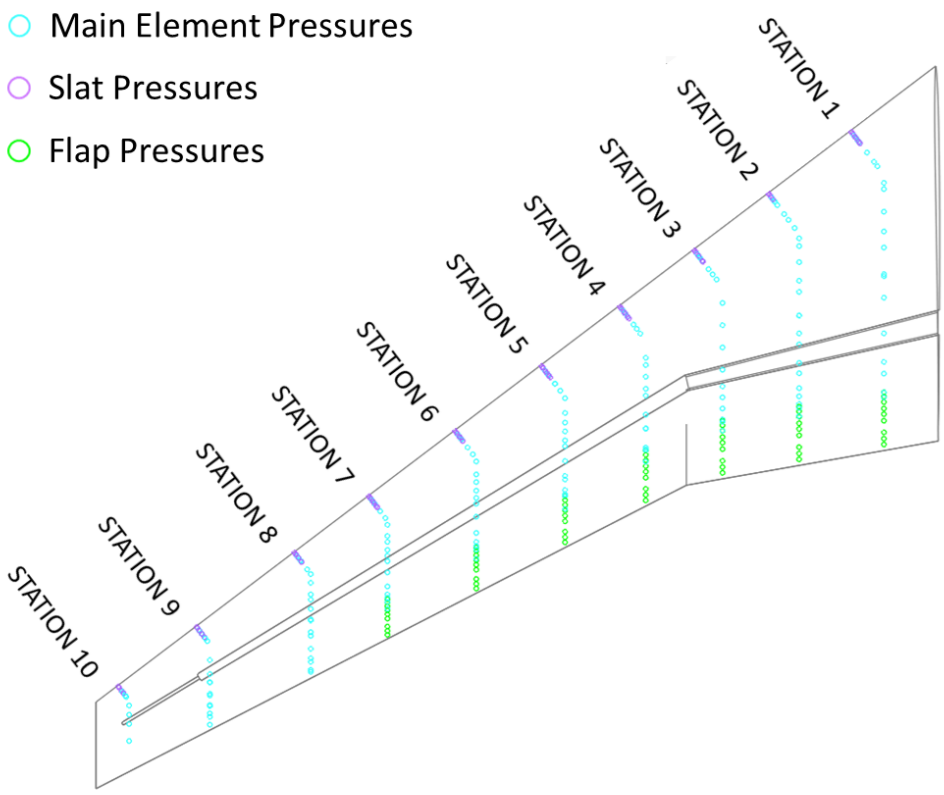


Fig. 8 Static pressure port locations on the 5.2%-scale CRM-HL wing.

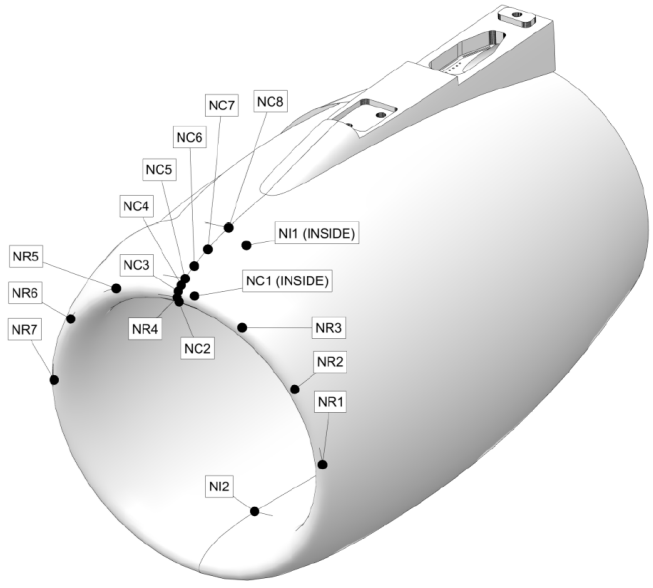


Fig. 9 Static pressure port locations on the 5.2%-scale CRM-HL nacelle.

IV. Test Matrix

To cover the maximum range of Reynolds numbers of interest, the NTF test campaign utilized both air and nitrogen modes. Using air mode enabled the capturing of data at low Reynolds numbers that could be directly compared to data taken at other atmospheric tunnels, while using nitrogen mode allowed for cryogenic testing at flight-like Reynolds numbers. Using both modes also gave the broadest data set to study Reynolds number trends and effects. Due to the NTF's unique ability to vary temperature and pressure independently, the test matrix also included Reynolds numbers that could be reached in both air and nitrogen mode allowing a comparison between modes. The ability to test at different dynamic pressures gave the capability to determine if there are any aeroelastic effects on the model. All Reynolds numbers referenced henceforth in this paper will refer to chord Reynolds numbers, based off the chord value given in Table 1. The test conditions for the landing configuration, which was the primary configuration of interest in this test, are shown in Table 5. The takeoff configuration was a secondary test objective, and therefore, had fewer test points. The test conditions for the takeoff configuration are shown in Table 6. Due to time constraints, the cruise configuration was not tested and will be studied in future test entries at the NTF. Data were collected over an alpha range of -4° to 22° using the pitch/pause method. Data were averaged over 4 seconds at a 40 hertz sampling rate.

Table 5 Nominal test conditions for the landing configuration of the 5.2%-scale CRM-HL.

Configuration	Mach	Chord Reynolds Number (Million)	Total Pressure (psia)	Temperature (°F)	q_∞ (psf)	Mode
Landing	0.20	1.61	15.5	95	61	Air
Landing	0.20	3.33	33.8	120	133	Air
Landing	0.20	5.49	52.6	100	207	Air
Landing	0.20	5.49	35.2	-50	138	Nitrogen
Landing	0.20	16	40.1	-250	157	Nitrogen
Landing	0.20	16	60.6	-180	240	Nitrogen
Landing	0.20	30	75.5	-250	295	Nitrogen

Table 6 Nominal test conditions for the takeoff configuration of the 5.2%-scale CRM-HL.

Configuration	Mach	Chord Reynolds Number (Million)	Total Pressure (psia)	Temperature (°F)	q_∞ (psf)	Mode
Takeoff	0.26	4.08	32.2	120	210	Air
Takeoff	0.26	1.97	15.6	120	101	Air
Takeoff	0.23	1.80	16.0	120	82	Air

V. Results and Discussion

All data shown have classical wall corrections applied. Wall interference corrections will be applied to all data via the Transonic Wall Interference Correction System (TWICS)[11], but those results were not yet available at the time of publication. However, historical data from semispan models of this scale tested in the NTF indicate that those corrections will be small in magnitude and are not likely to affect the trends of the data.

A. Baseline Landing Configuration Force and Moment Results

The lift, drag, and pitching moment coefficients as a function of angle of attack (α) and the drag polar for the landing configuration in air mode are shown in Figure 10. The lift curves followed the expected trend of increasing lift as the Reynolds number increased. At the negative angles of attack and the higher (positive) angles of attack, the drag curves decreased with increasing Reynolds number. The 1.6 million chord Reynolds number run corresponded to prior testing of the 5.2%-scale CRM-HL model in the 14x22 and NWB wind tunnels and showed good test-to-test and tunnel-to-tunnel agreement [5, 6]. The 3.32 and 5.49 million chord Reynolds number runs showed a clear difference in behavior above $C_{L,max}$.

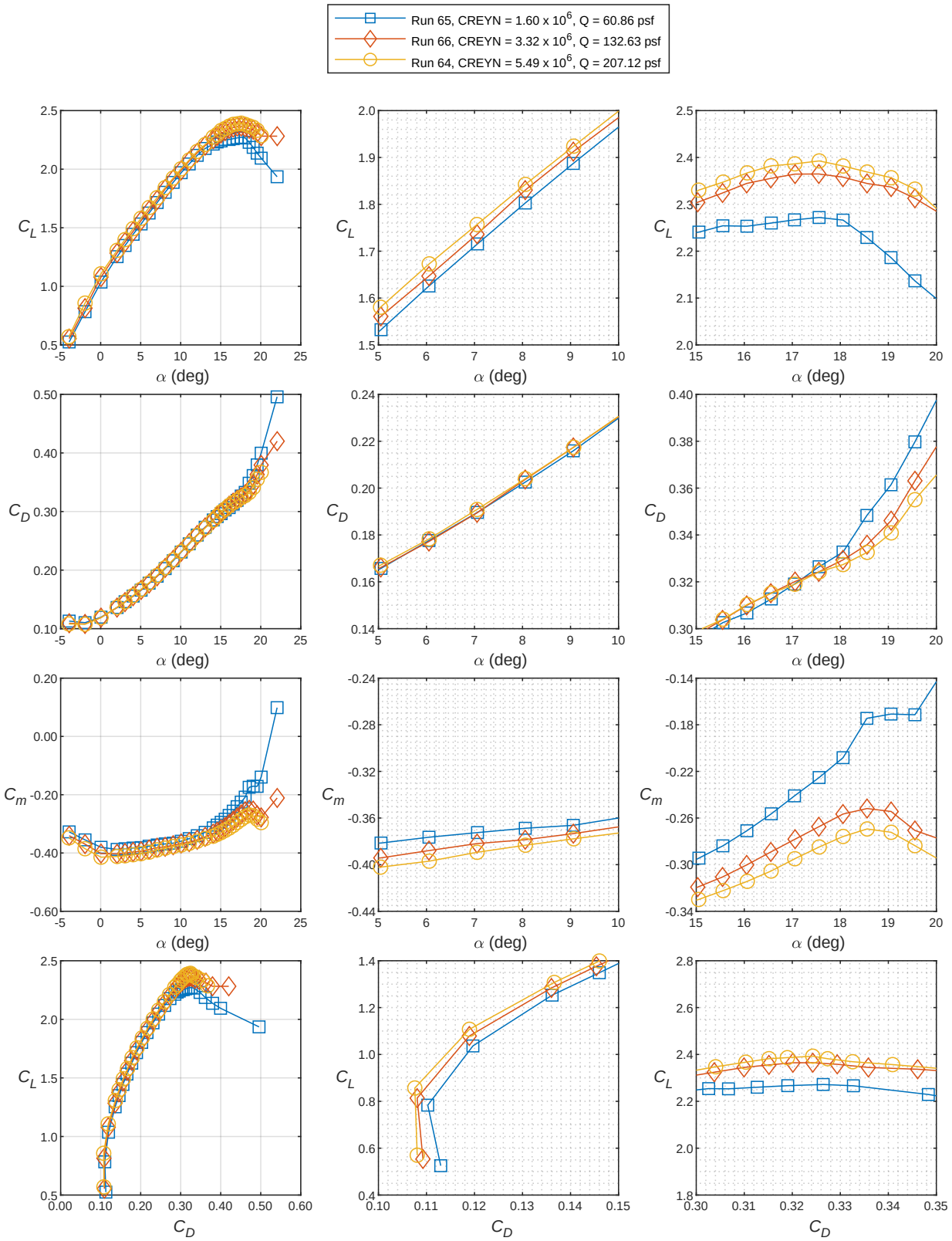


Fig. 10 Lift, drag, and pitching moment plotted against angle of attack, and the drag polar for the landing configuration in air mode, $M_\infty = 0.20$.

The lift, drag, and pitching moment coefficients as a function of angle of attack (α) and the drag polar for the landing configuration in cryogenic nitrogen mode are shown in Figure 11. Comparing the 5.49 million chord Reynolds number lift curve with the 16 and 30 million chord Reynolds number lift curves the data did not follow the expected trend of increasing lift as the chord Reynolds number increases. Not only was the 5.49 million chord Reynolds number lift curve higher than both the 16 and 30 million chord Reynolds number curves in a significant portion of the linear range before $C_{L,max}$, there was a much smaller difference in the lift curves than may be expected between the 16 and 30 million runs. There was also an unexpected result at the negative angles of attack on the lift curve where the 16 million chord Reynolds number run was higher than the 30 million chord Reynolds number run. This difference in the lift curves was outside the bounds of the balance uncertainty. The drag coefficient was lowest for the 5.49 million chord Reynolds number run. Additionally, the drag coefficient did not have a consistent trend when comparing the 30 million chord Reynolds number run to the 16 million chord Reynolds number run. A large difference in the pitching moment curves was seen across the angle of attack range for the chord Reynolds numbers tested. Generally the boundary layer on the wing decreases in thickness with an increase in chord Reynolds number, which in turn leads to an increase in the lift curve by increasing the effective camber of the wing [12, 13]. However, the data presented herein have differing dynamic pressures as well as differing chord Reynolds numbers. There is a possibility aeroelastic effects on the wing, due to increasing dynamic pressure, may be canceling out the Reynolds number effect as a reduction in wing twist would lead to a reduction in lift. Preliminary analysis of wing deformation data (including wing twist and deflection) collected during the test entry has shown wing twist and tip deflection to have been small in magnitude. Dynamic pressure comparisons will follow in the text, and will also show aeroelastic effects on the wing were likely small for the cases presented. Nevertheless, the aeroelastic effects and Reynolds number effects canceling each other out has been seen in previous testing of other CRM variants in NTF [12] and should be mentioned as a possible explanation.

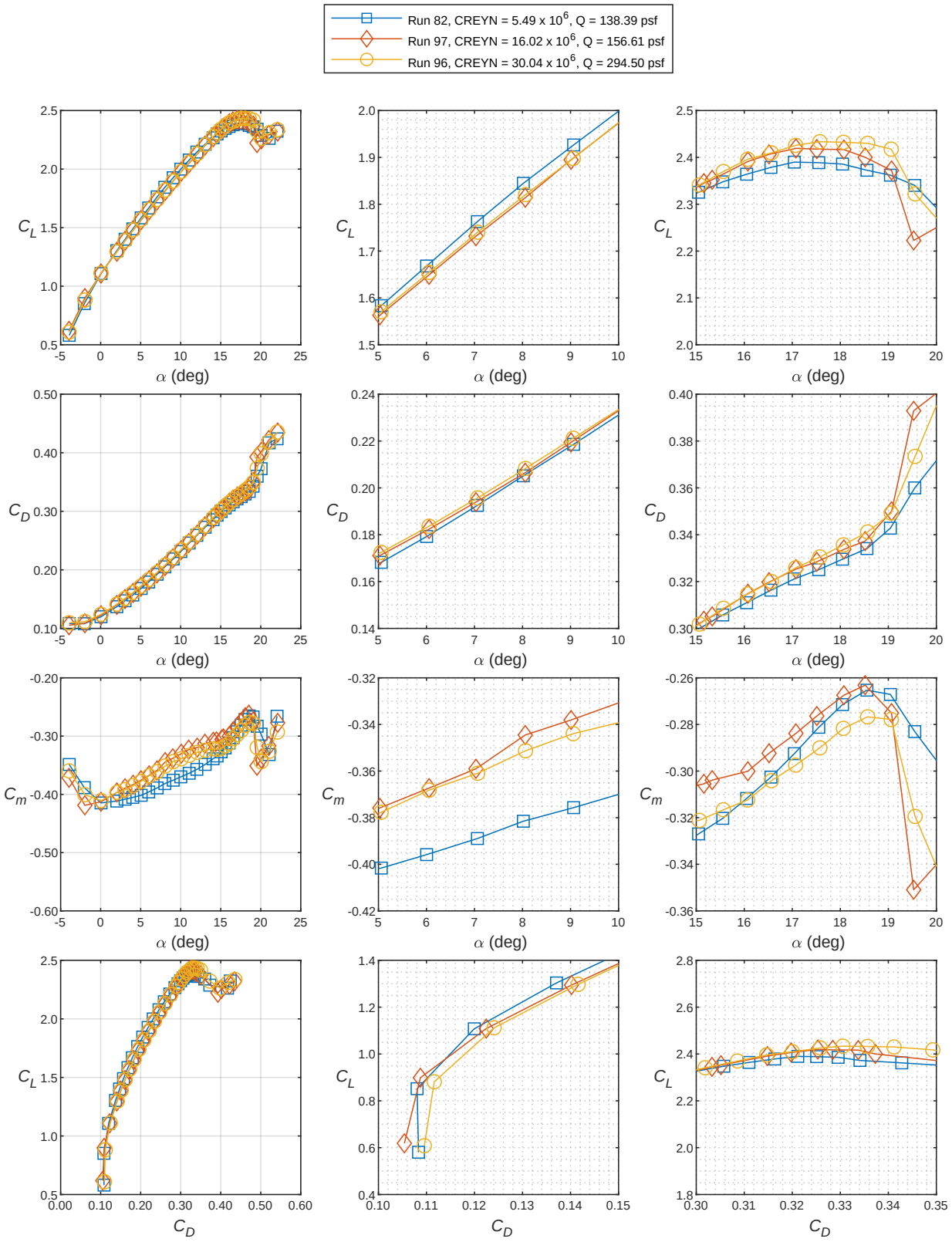


Fig. 11 Lift, drag, and pitching moment plotted against angle of attack, and the drag polar for the landing configuration in cryogenic nitrogen mode, $M_\infty = 0.20$.

The lift, drag, and pitching moment coefficients as a function of angle of attack (α) and the drag polar for the landing configuration at all Reynolds numbers tested are shown in Figure 12. The 5.49 million chord Reynolds number runs completed in both air and nitrogen modes (Runs 64 and 82 in the figure) showed good agreement in lift, drag, and pitching moment. This close agreement for this specific comparison pointed toward an insensitivity to aeroelastic effects, which was in line with pretest predictions and the intended model design. However, as mentioned above, the 16 and 30 million chord Reynolds number cases appear to have some level of aeroelastic effects based on the trends in the data in the linear region of the lift, drag, and pitching moment curves. $C_{L,max}$ trended upward with increasing Reynolds number, shown in Figure 13.

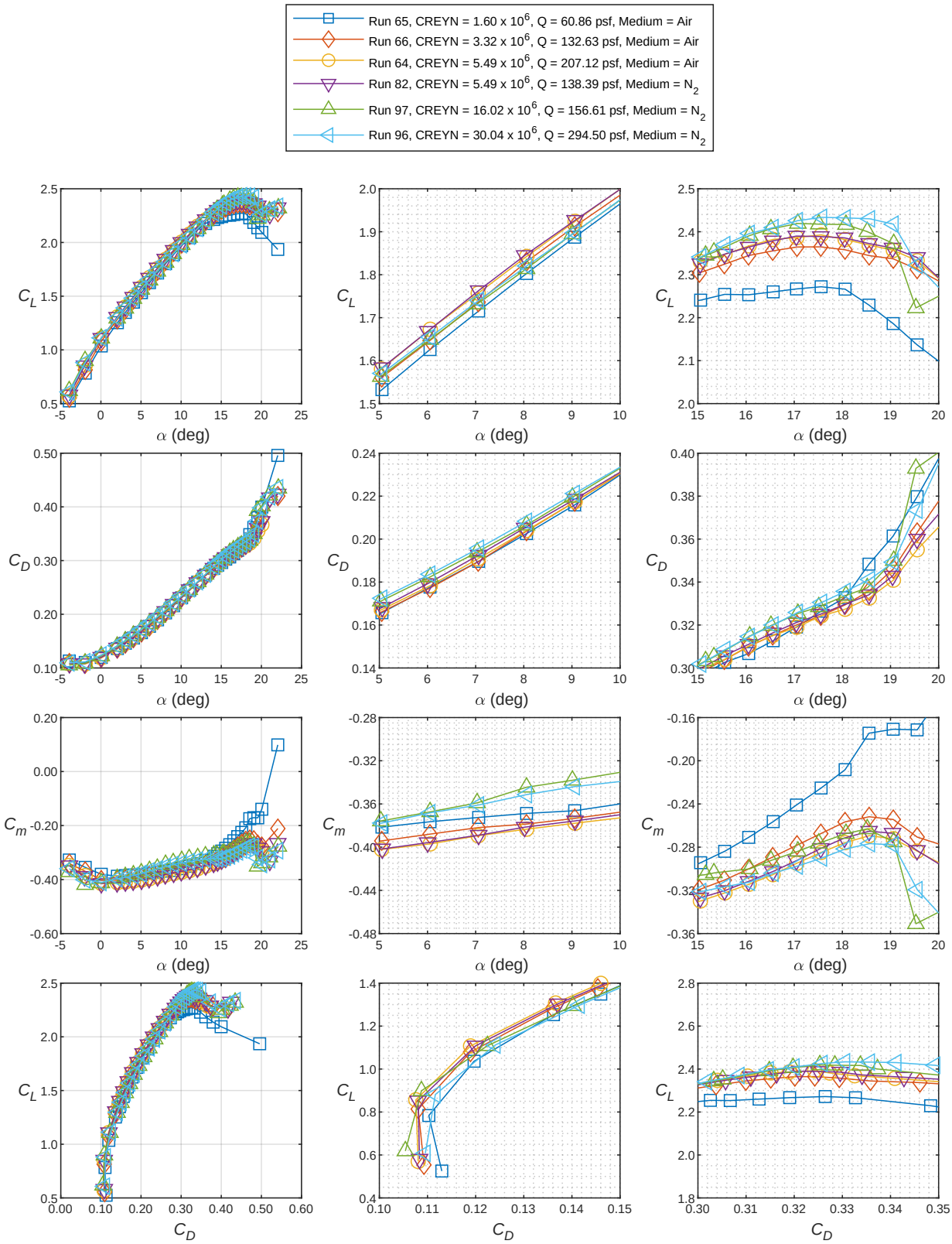


Fig. 12 Lift, drag, and pitching moment plotted against angle of attack, and the drag polar for the landing configuration for all chord Reynolds numbers tested, $M_\infty = 0.20$.

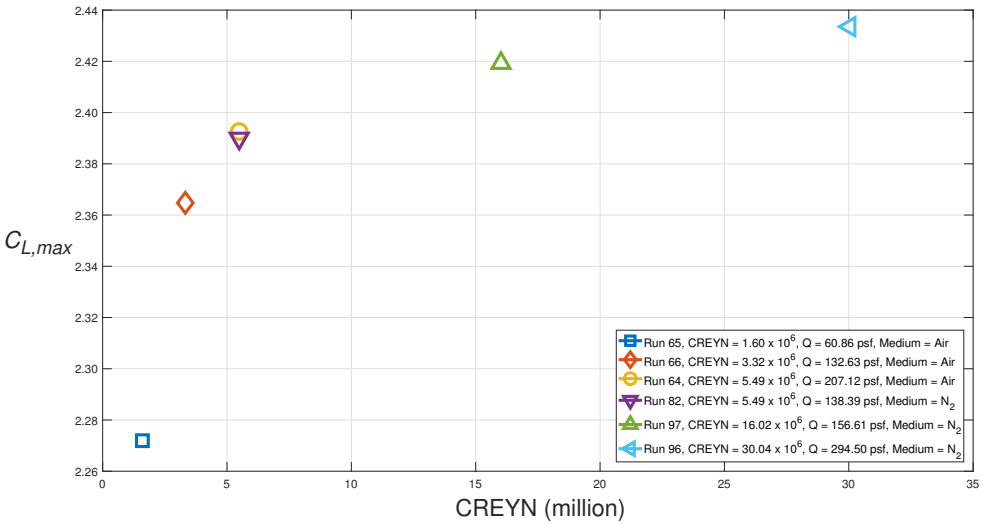


Fig. 13 $C_{L,max}$ trend with chord Reynolds number in the landing configuration, $M_\infty = 0.20$.

Focusing on the potential effects of dynamic pressure, Figure 14 shows the behavior of pairs of runs at the 5.49 and 16 million chord Reynolds number. Runs 64 and 82 were both at 5.49 million with an approximate 70 psf dynamic pressure difference and runs 97 and 94 were both near 16 million with an approximate 80 psf dynamic pressure difference. Of note, the 5.49 million chord Reynolds number runs compared well between the air and nitrogen test mediums. The model was designed to be insensitive to dynamic pressure effects at the planned test conditions. Lift and drag appeared to be insensitive to dynamic pressure effects below and at $C_{L,max}$, with slight differences post stall at both the 5.49 and 16 million chord Reynolds number conditions. Potential aeroelastic changes in the twist and deflection of the wing may have affected the pitching moment curves at the 16 million chord Reynolds number condition.

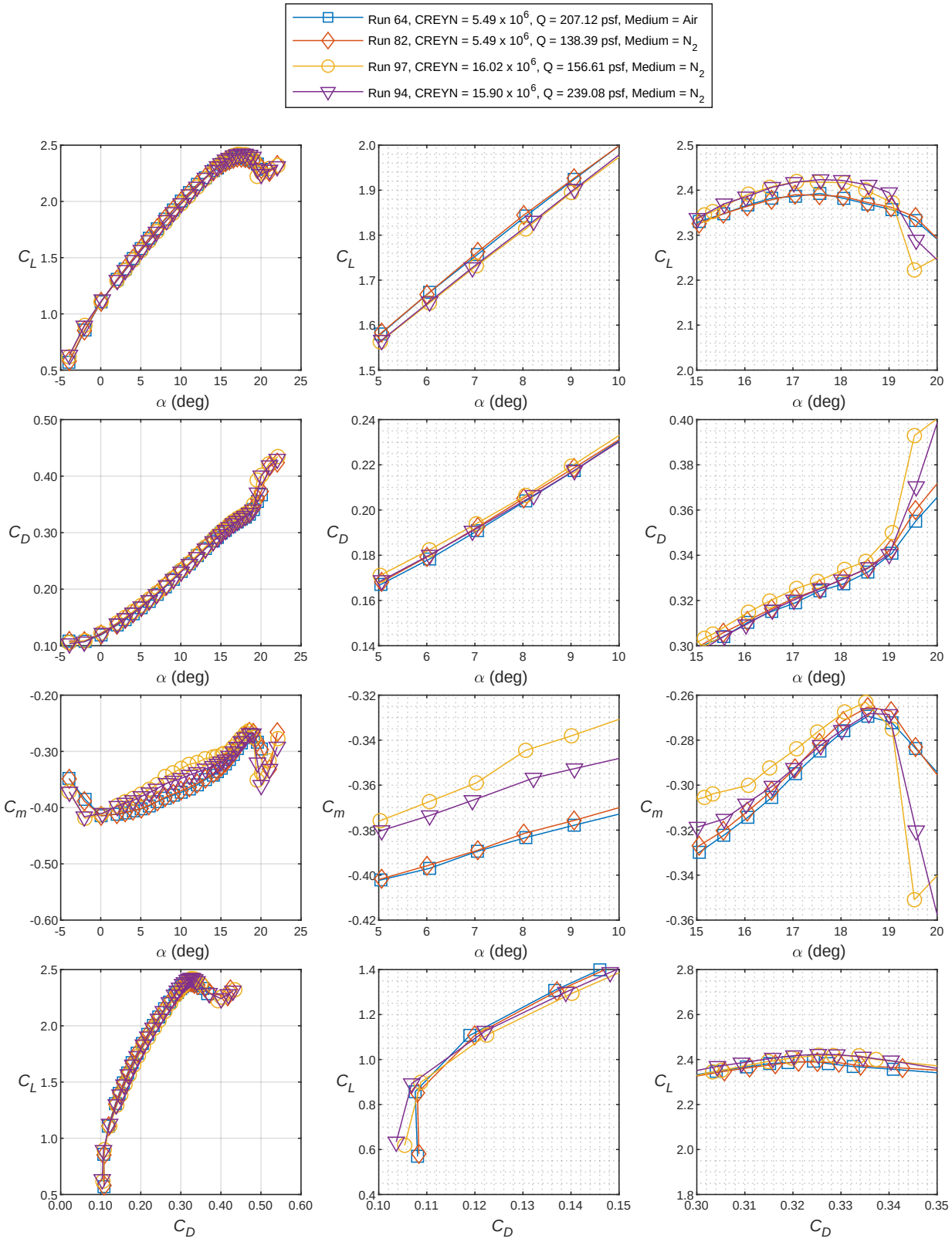


Fig. 14 Lift, drag, and pitching moment plotted against angle of attack, and the drag polar for the landing configuration comparing differing dynamic pressures at 5.49 and 16 million chord Reynolds numbers, $M_\infty = 0.20$.

B. Component Effect Force and Moment Results

The following figures and discussion will show the effect of the nacelle, landing gear, and horizontal tail on the lift, drag, and pitching moment curves of the model and how those effects change with Reynolds number. In general, there were mild sensitivities to Reynolds number with component increments.

The lift, drag, and pitching moment coefficients as a function of angle of attack (α) and the drag polar for the landing configuration with and without the landing gear installed in air mode are shown in Figure 15. As predicted, the landing gear overall increased drag and lowered lift at both chord Reynolds numbers tested. The pitching moment increased at both chord Reynolds numbers with the gear installed. Comparing the lift, drag, and pitching moment curves and drag polar for the landing gear "off" runs versus the landing gear "on" runs indicated there was slightly more sensitivity to Reynolds number on the lift and pitching moment in the linear region with the landing gear off. Also, there was slightly more sensitivity to Reynolds number seen with drag at the highest angles of attack with landing gear on.

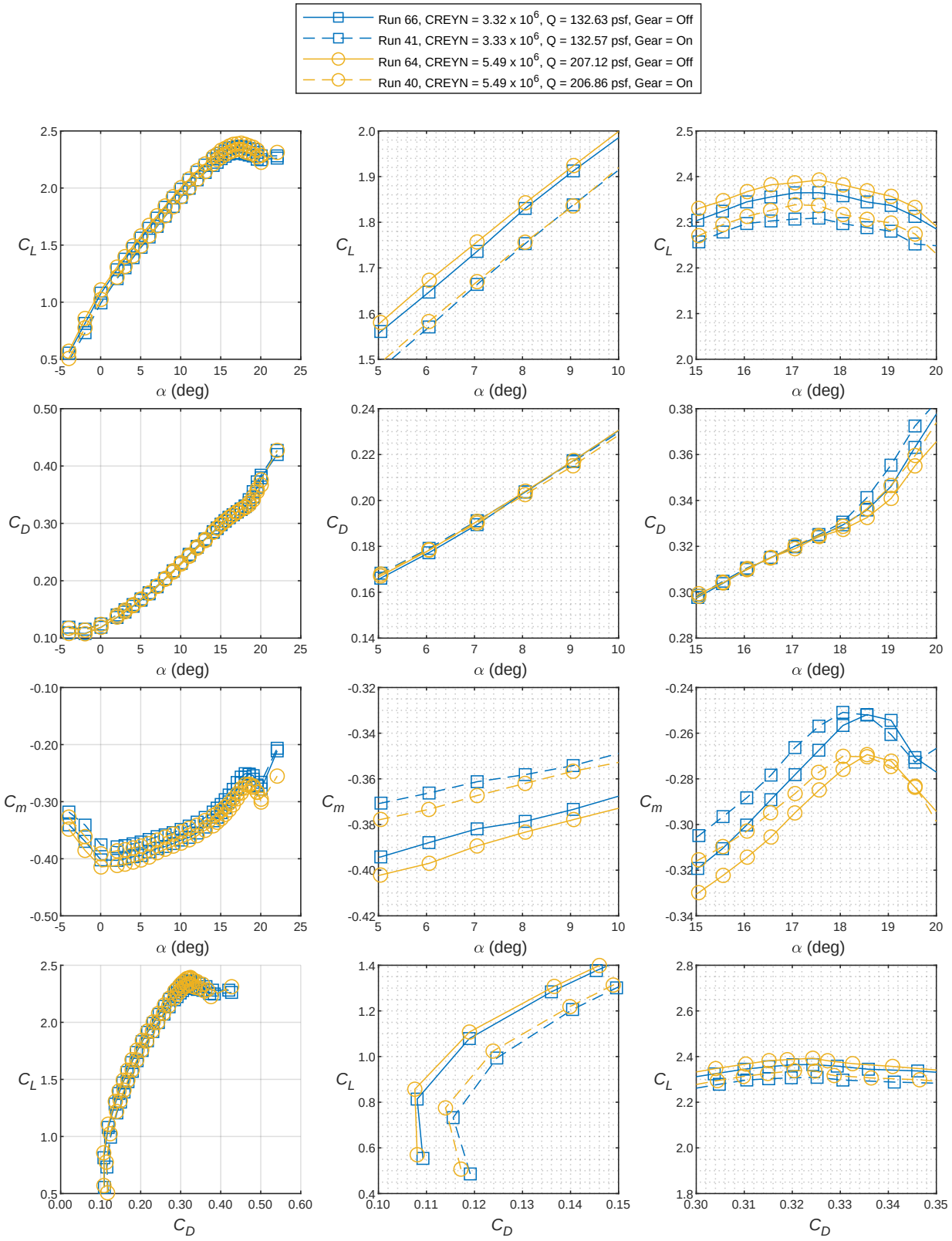


Fig. 15 Lift, drag, and pitching moment plotted against angle of attack, and the drag polar for the landing configuration with and without the landing gear in air mode at lower chord Reynolds numbers, $M_\infty = 0.20$.

The lift, drag, and pitching moment coefficients as a function of angle of attack (α) and the drag polar for the landing configuration with and without the nacelle installed in air mode are shown in Figure 16. As noted previously, the nacelle included a chine during the test. The same comparison is shown for the configuration in nitrogen mode in Figure 17. With the addition of the nacelle, the lift, drag, and pitching moment increased across most of the positive angle of attack range (with the exception of the lift curve near stall and post stall). This behavior was consistent with prior CRM testing [12]. For the "nacelle off" configuration, the $C_{L,max}$ occurred at a higher angle of attack than the "nacelle on" configuration. The pitching moment was the most sensitive to the addition of the nacelle. For all cases, some mild sensitivity to Reynolds number was seen on the lift, drag, and pitching moment with nacelle off versus nacelle on. In Figure 16, in the linear region slightly more sensitivity was seen with nacelle on for lift, and at the higher angles of attack region slightly more sensitivity was seen with nacelle off for lift and pitching moment. In Figure 17, in the linear region more sensitivity was seen with nacelle off for lift and pitching moment. At the higher angles of attack region more sensitivity was seen with nacelle on for lift and more sensitivity was seen with nacelle off for drag and pitching moment. At high angles of attack, inconsistent trends in the drag coefficient were seen depending on if the nacelle was on or off between the lower and higher chord Reynolds numbers.

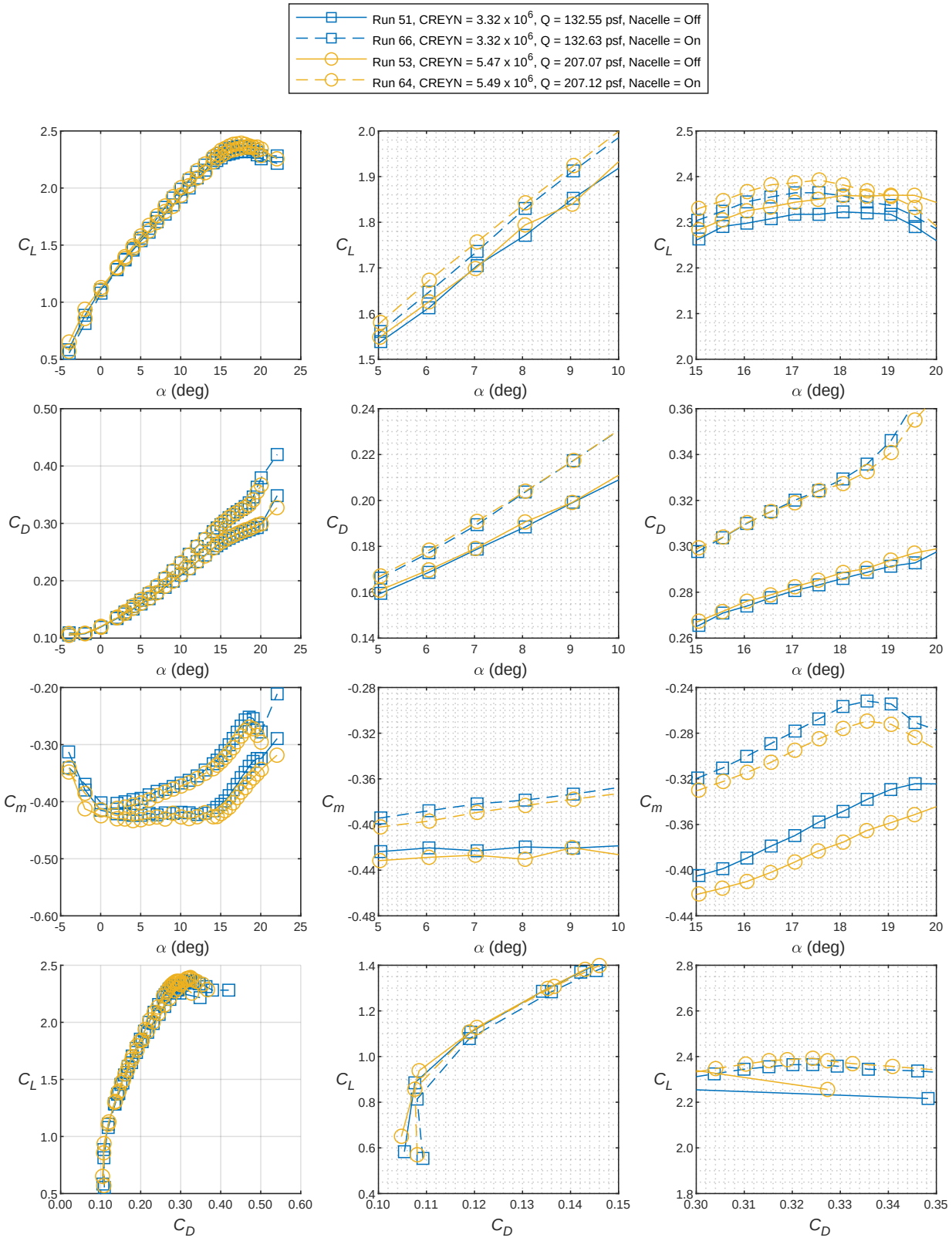


Fig. 16 Lift, drag, and pitching moment plotted against angle of attack, and the drag polar for the landing configuration with and without the nacelle in air mode at lower chord Reynolds numbers, $M_\infty = 0.20$.

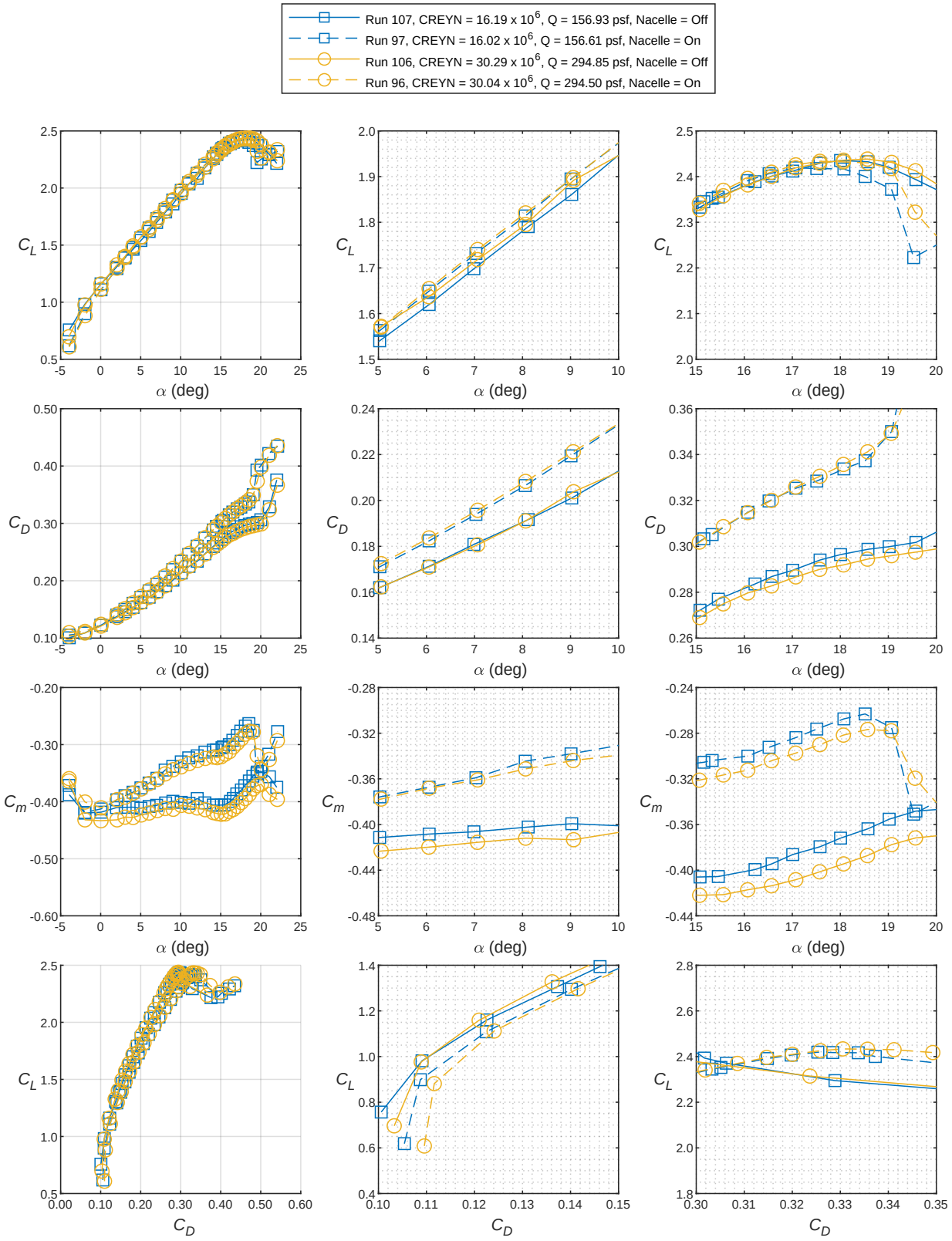


Fig. 17 Lift, drag, and pitching moment plotted against angle of attack, and the drag polar for the landing configuration with and without the nacelle in nitrogen mode at higher chord Reynolds numbers, $M_\infty = 0.20$.

The lift, drag, and pitching moment coefficients as a function of angle of attack (α) and the drag polar for the landing configuration with and without the horizontal tail installed in air mode are shown in Figure 18. The same comparison is shown for the configuration in nitrogen mode in Figure 19. The addition of the horizontal tail changed the sign on the slope of the pitching moment, as expected for a tube and wing aircraft configuration. The change in slope in the lift curves was likely due to the horizontal tail being untrimmed. At the higher angles of attack, near stall, the lift was shown to increase with horizontal tail on. Trends in the drag and pitching moment were inconsistent between the lower and higher chord Reynolds numbers. In Figure 19, trends in lift in the linear region for horizontal tail off were different that what would be expected, lift decreased with the increase in Reynolds number. At the higher chord Reynolds numbers in Figure 19, horizontal tail off was marginally more sensitive to Reynolds number on lift and pitching moment in the linear region, and horizontal tail on was slightly more sensitive to lift and pitching moment at the higher angles of attack. For both the low and high sets of chord Reynolds numbers, the "with tail" configuration was more sensitive in pitching moment for the higher angle of attack range.

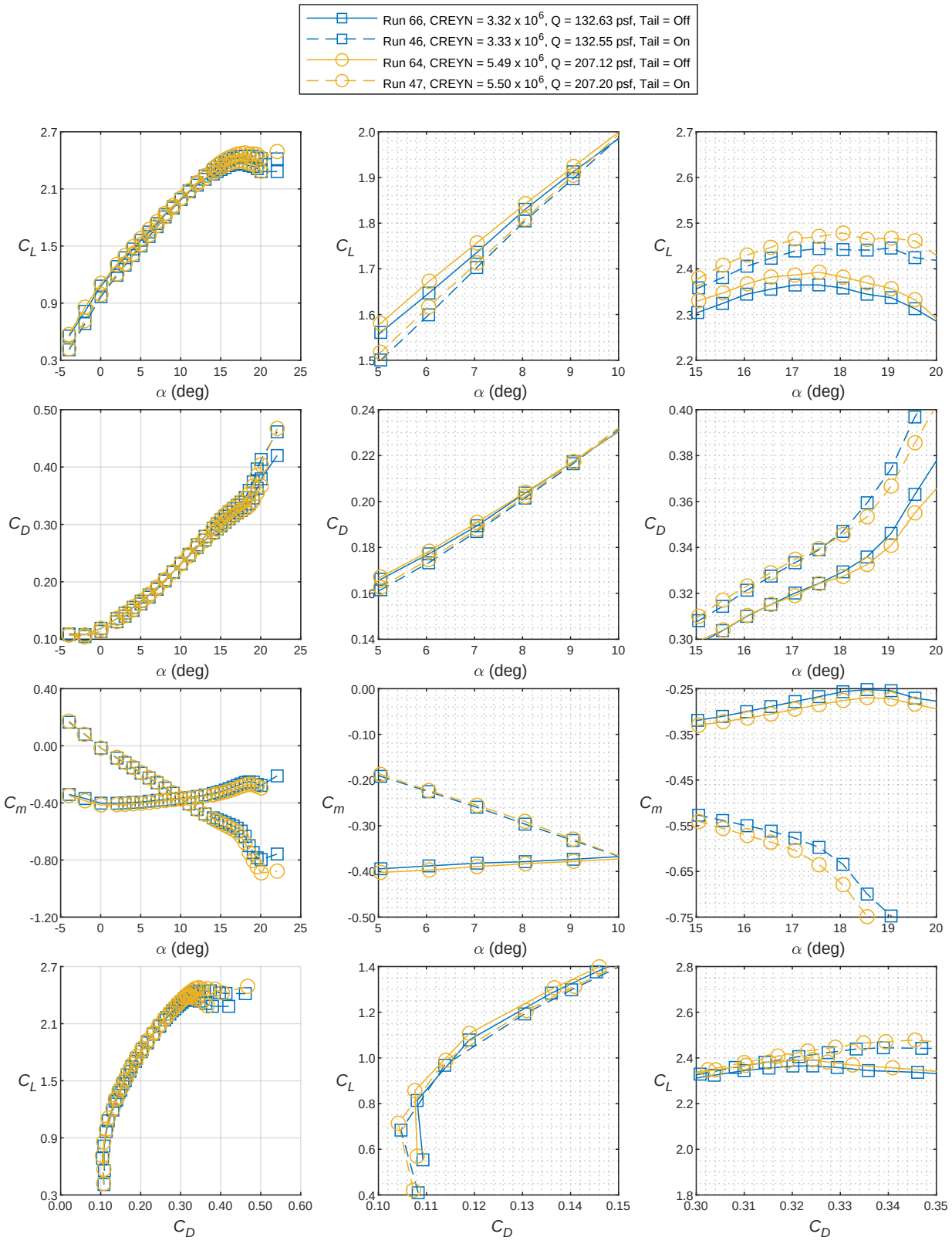


Fig. 18 Lift, drag, and pitching moment plotted against angle of attack, and the drag polar for the landing configuration with and without the horizontal tail in air mode at lower chord Reynolds numbers, $M_\infty = 0.20$.

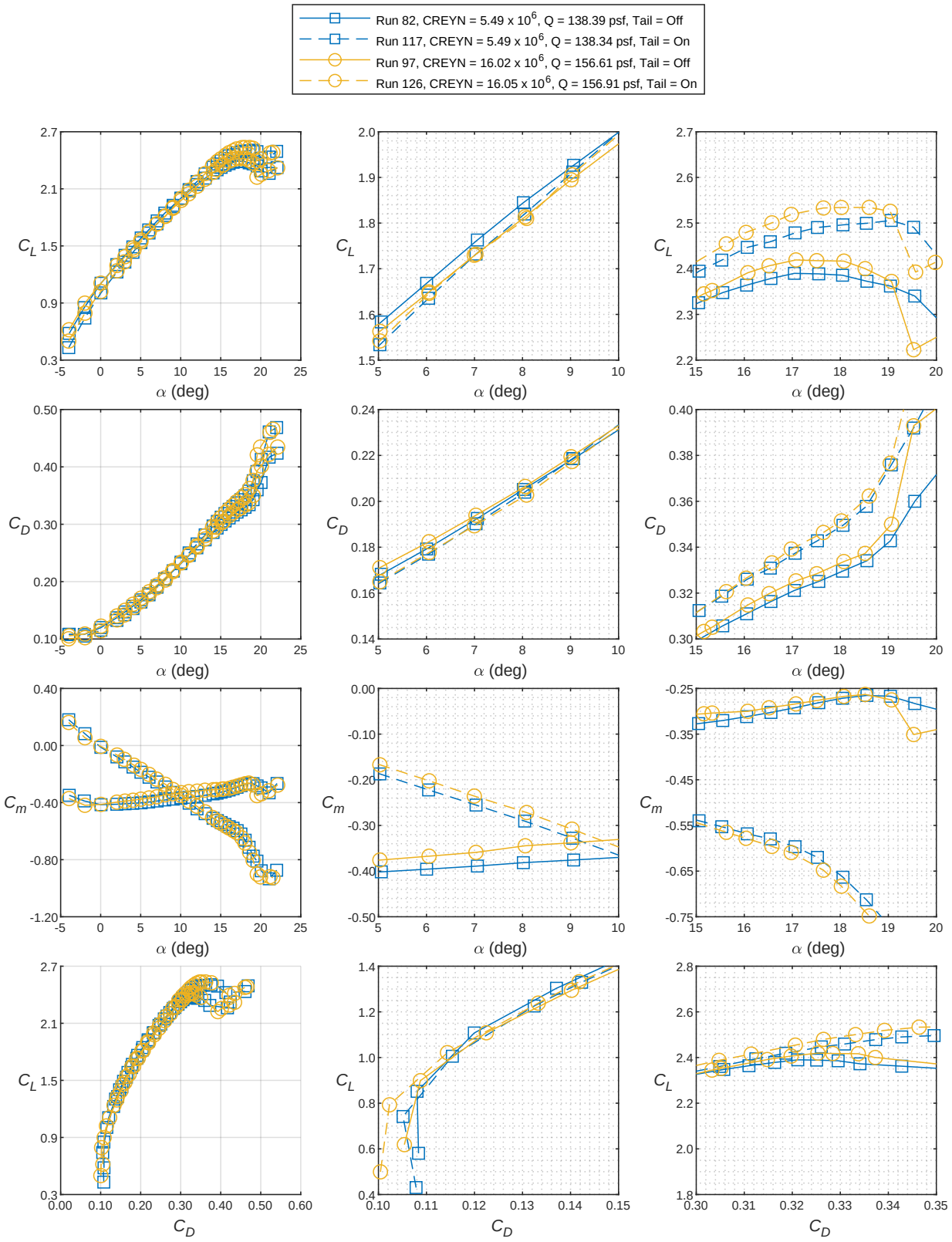


Fig. 19 Lift, drag, and pitching moment plotted against angle of attack, and the drag polar for the landing configuration with and without the horizontal tail in nitrogen mode at higher chord Reynolds numbers, $M_\infty = 0.20$.

C. Takeoff Configuration Force and Moment Results

Due to test time and facility limitations, the model was only tested in the takeoff configuration in warm nitrogen mode at lower Reynolds numbers. The slat and flap deflections were set to 22° and 25° respectively. Both angles were a reduction in magnitude as compared to the landing configuration, shown in Table 2. The test conditions also differed with the Mach number increased to 0.26, altering the Reynolds numbers as shown in Table 6. The lift, drag, and pitching moment coefficients as a function of angle of attack (α) and the drag polar for the takeoff configuration in warm nitrogen mode are shown in Figure 20. Run 164 was at an alternate Mach number of 0.23 to provide a comparison to data taken at The German Aerospace Center (DLR) NWB facility that could not reach the CRM-HL ecosystem suggested Mach number of 0.26. Like the landing configuration, the results followed the expected trend of lift increasing with increasing Reynolds number, particularly an increase in $C_{L,max}$. Looking at the constant Mach number cases (Mach = 0.26), some sensitivity to Reynolds number was seen on lift and pitching moment for the entire angle of attack range. Reynolds number sensitivity was seen for drag only at the higher angles of attack. While Runs 162 and 164 were at different Mach numbers, the resulting Reynolds number difference was small with fairly close agreement in lift and drag in the pre-stall range.

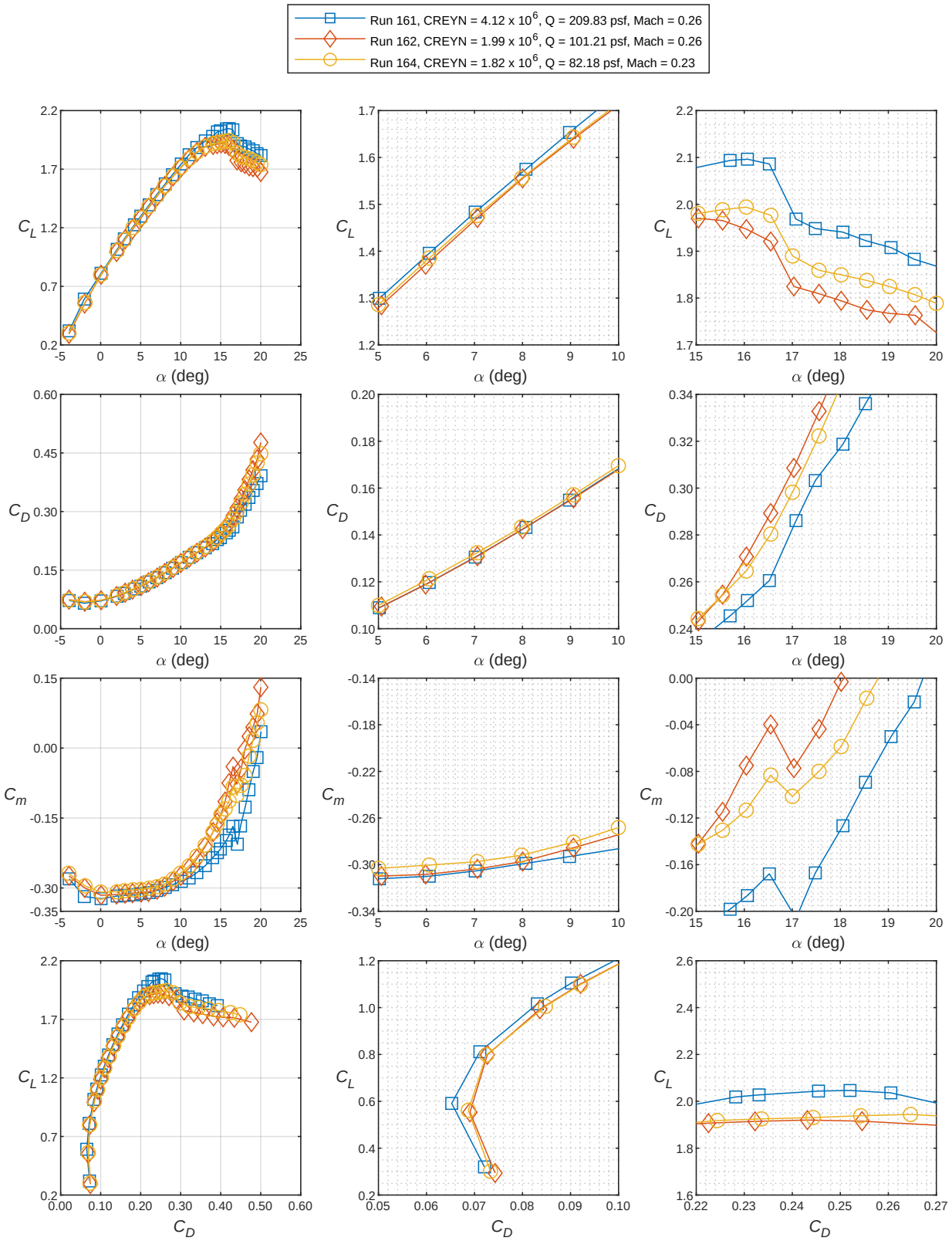


Fig. 20 Lift, drag, and pitching moment plotted against angle of attack, and the drag polar for the takeoff configuration in warm nitrogen mode, $M_\infty = 0.23 - 0.26$.

D. Preliminary Landing Configuration Surface Pressure Results

The wind tunnel model was instrumented with surface pressure ports on the slat, main element, and flaps as described in Figure 8. The lift curves of the selected runs of interest are shown in Figure 21. The measured surface pressures on the slat, main element, and flaps in the landing configuration for a range of angles of attack from 8° to 20° are shown at an inboard location (Station 1) in Figures 22 through 24. The same set of angles of attack are shown for a midspan and outboard wing station (Stations 4 and 7) in Figures 25 though 27 and Figures 28 though 30 respectively. Additional angles of attack were studied, but only a representative subset will be shown in this publication. The coefficient of pressure is plotted versus the x location in the model wing coordinate system. The symbols on the plot reference the pressure locations on the slat (x), main element (o), and flap (*). Because the wing was in a deployed configuration, some pressures were at the same x coordinate location due to being on the upper or lower surface or within the cove of the deployed surfaces. Also note, ahead of the 25% local wing chord, the pressure ports were perpendicular to the leading edge. Five different chord Reynolds numbers are plotted in the figures, denoted by different colors, to highlight the effect of Reynolds numbers on the surface pressures. Each figure represents a different angle of attack. Data that are presented at the angle of attack of 8° were within the linear range of the lift curve, well before $C_{L,max}$ and stall. Data presented at angles of attack at 18° capture the behavior near $C_{L,max}$. Data presented at an angle of attack of 20° shows the behavior post stall. A gap in the main element pressures Figures 28 through 30, can be attributed to a nonfunctioning pressure port on the lower surface of the main element at Station 7. The results and discussion of surface pressures are considered preliminary, as more detailed analysis and reporting will be the subject of future publications.

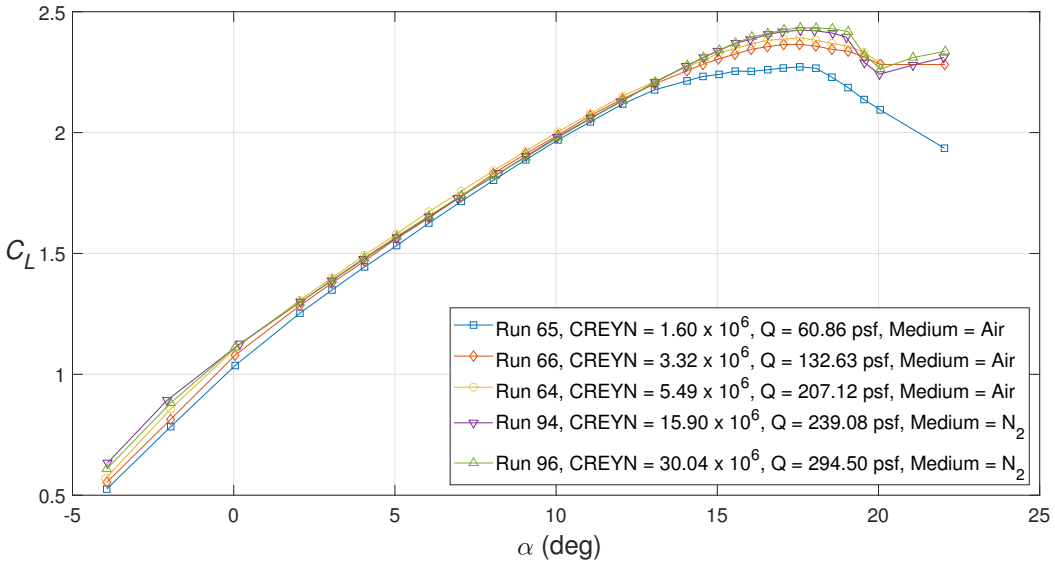


Fig. 21 Comparison of the lift curves for the landing configuration at varying chord Reynolds numbers, $M_\infty = 0.2$.

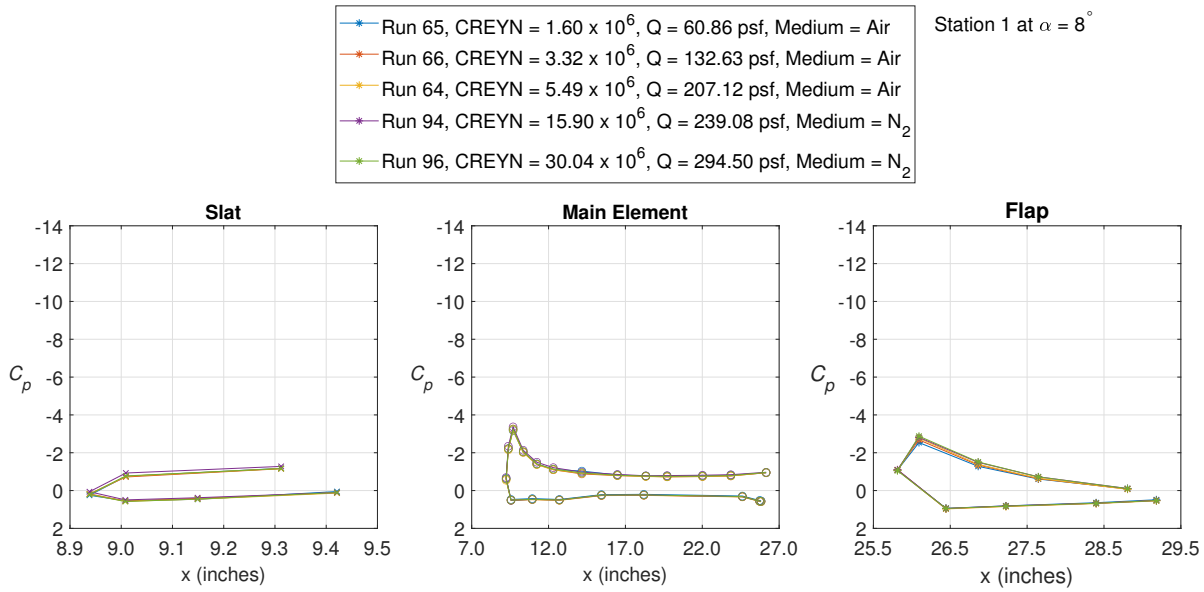


Fig. 22 Surface pressure coefficients at inboard wing station 1 in the landing configuration at varying chord Reynolds numbers at an angle of attack of $8°$, $M_\infty = 0.2$ (dimensions in model wing coordinate system, symbols indicate location: slat = x, main element = o, flap = *).

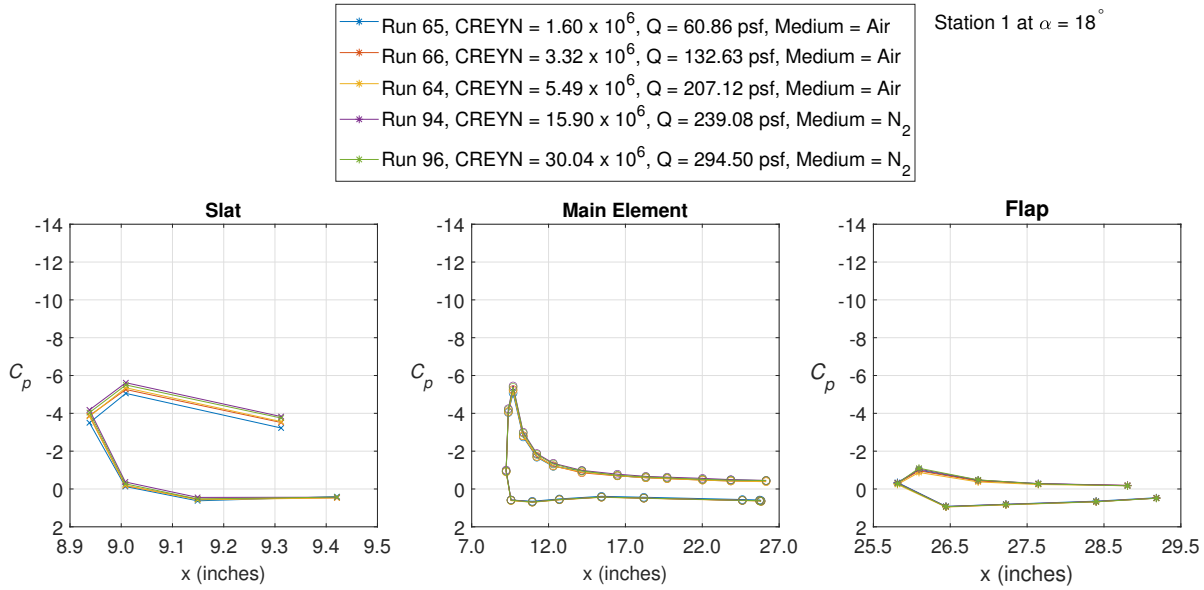


Fig. 23 Surface pressure coefficients at inboard wing station 1 in the landing configuration at varying chord Reynolds numbers at an angle of attack of $18°$, $M_\infty = 0.2$ (dimensions in model wing coordinate system, symbols indicate location: slat = x, main element = o, flap = *).

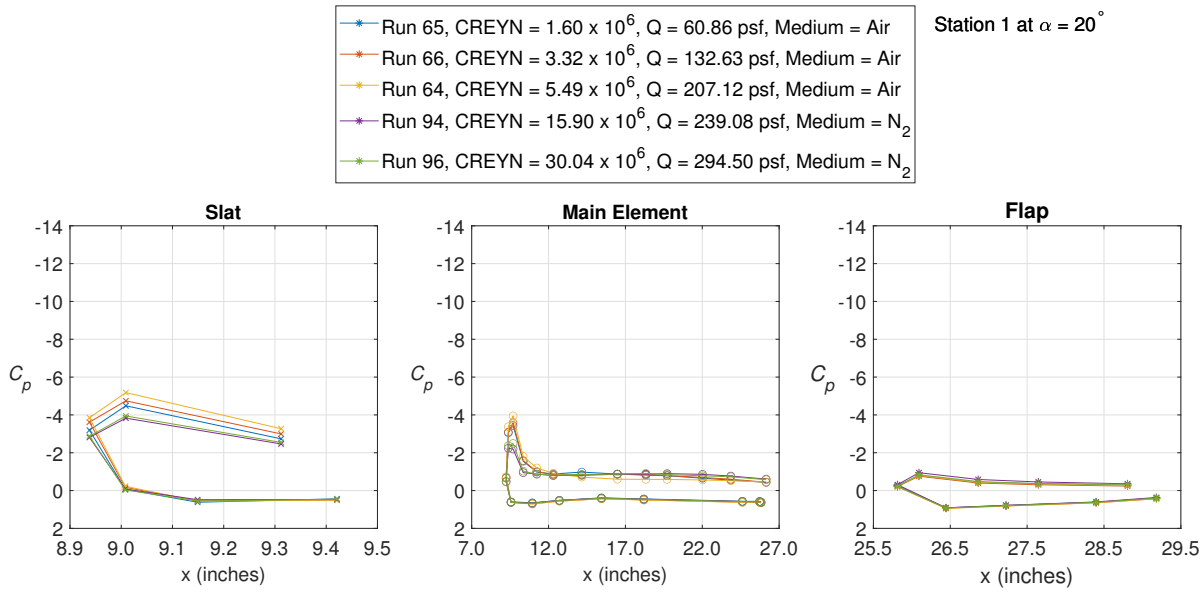


Fig. 24 Surface pressure coefficients at inboard wing station 1 in the landing configuration at varying chord Reynolds numbers at an angle of attack of $20°$, $M_\infty = 0.2$ (dimensions in model wing coordinate system, symbols indicate location: slat = x, main element = o, flap = *).

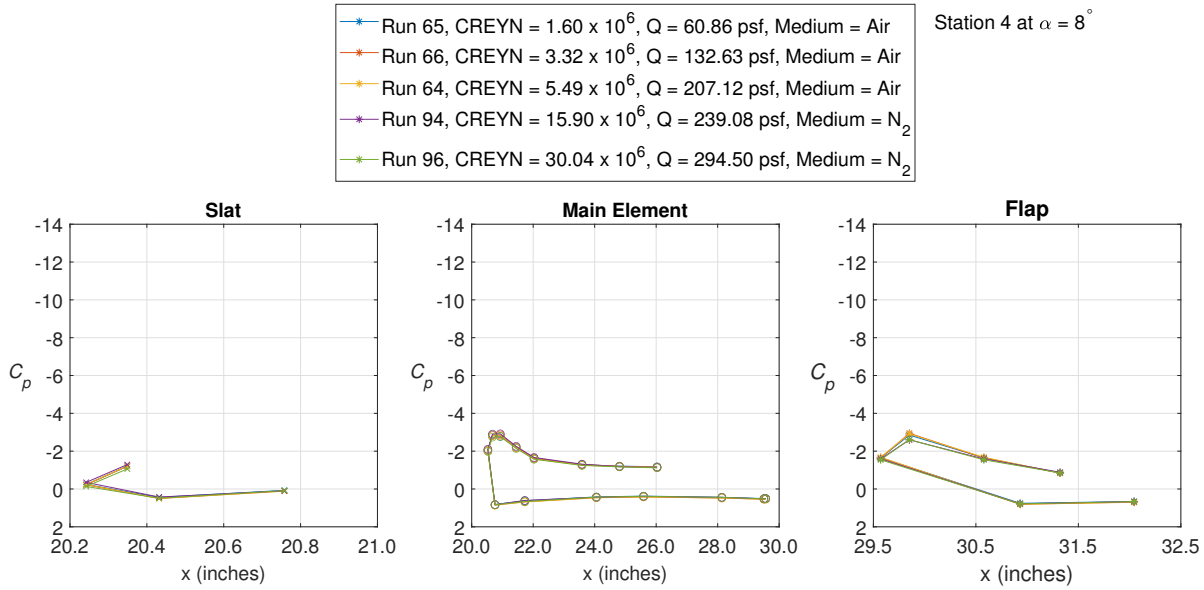


Fig. 25 Surface pressure coefficients at midspan wing station 4 in the landing configuration at varying chord Reynolds numbers at an angle of attack of $8°$, $M_\infty = 0.2$ (dimensions in model wing coordinate system, symbols indicate location: slat = x, main element = o, flap = *).

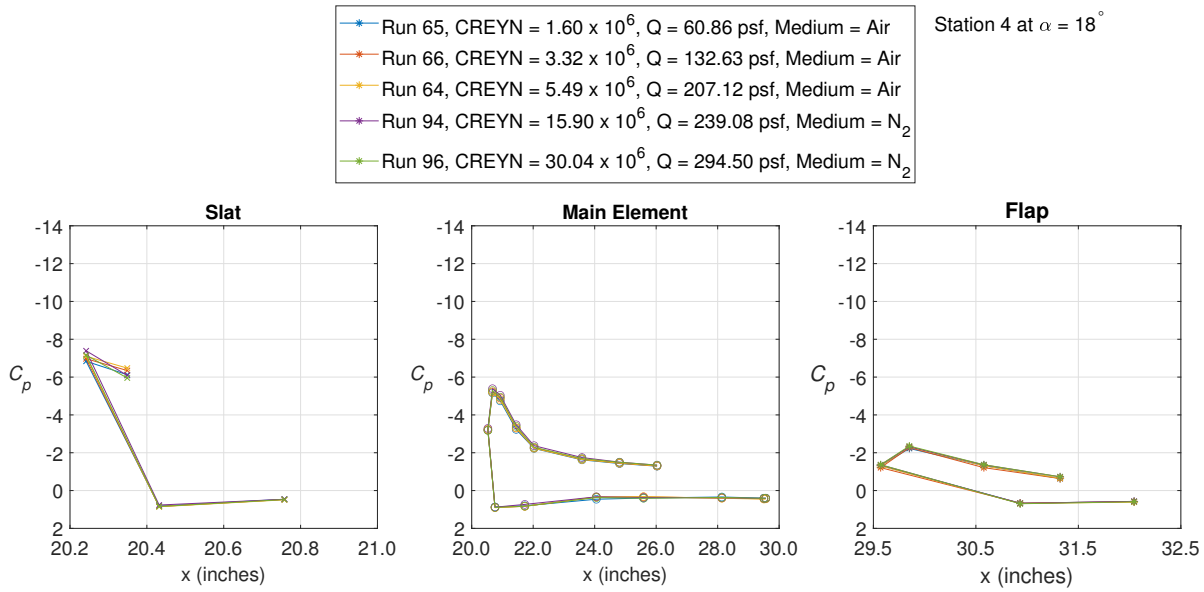


Fig. 26 Surface pressure coefficients at midspan wing station 4 in the landing configuration at varying chord Reynolds numbers at an angle of attack of $18°$, $M_\infty = 0.2$ (dimensions in model wing coordinate system, symbols indicate location: slat = x, main element = o, flap = *).

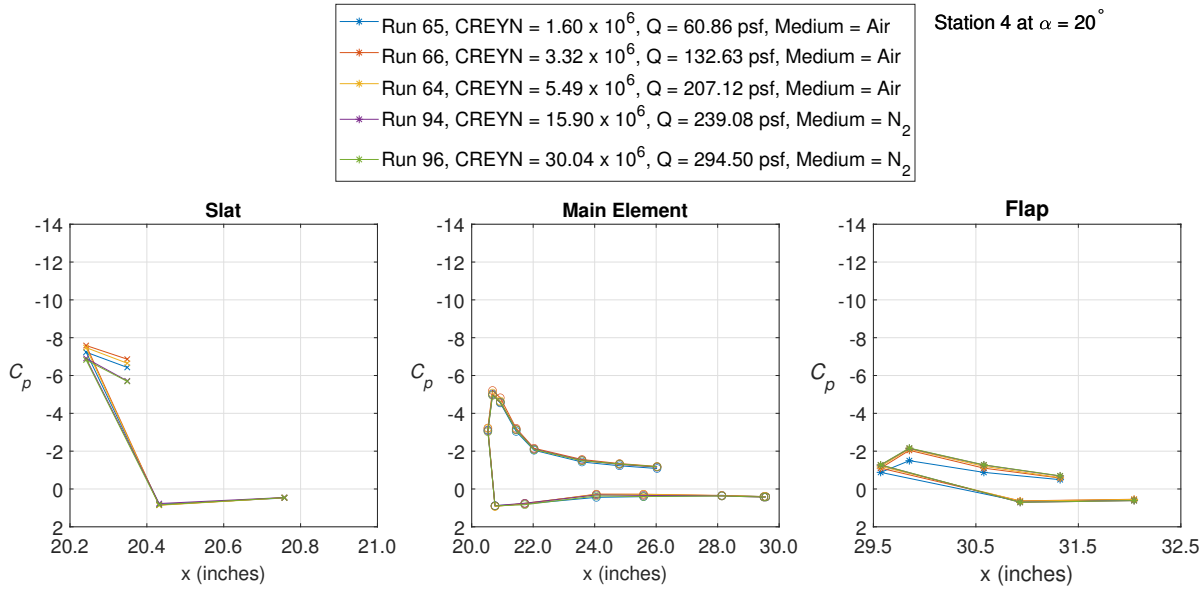


Fig. 27 Surface pressure coefficients at midspan wing station 4 in the landing configuration at varying chord Reynolds numbers at an angle of attack of $20°$, $M_\infty = 0.2$ (dimensions in model wing coordinate system, symbols indicate location: slat = x, main element = o, flap = *).

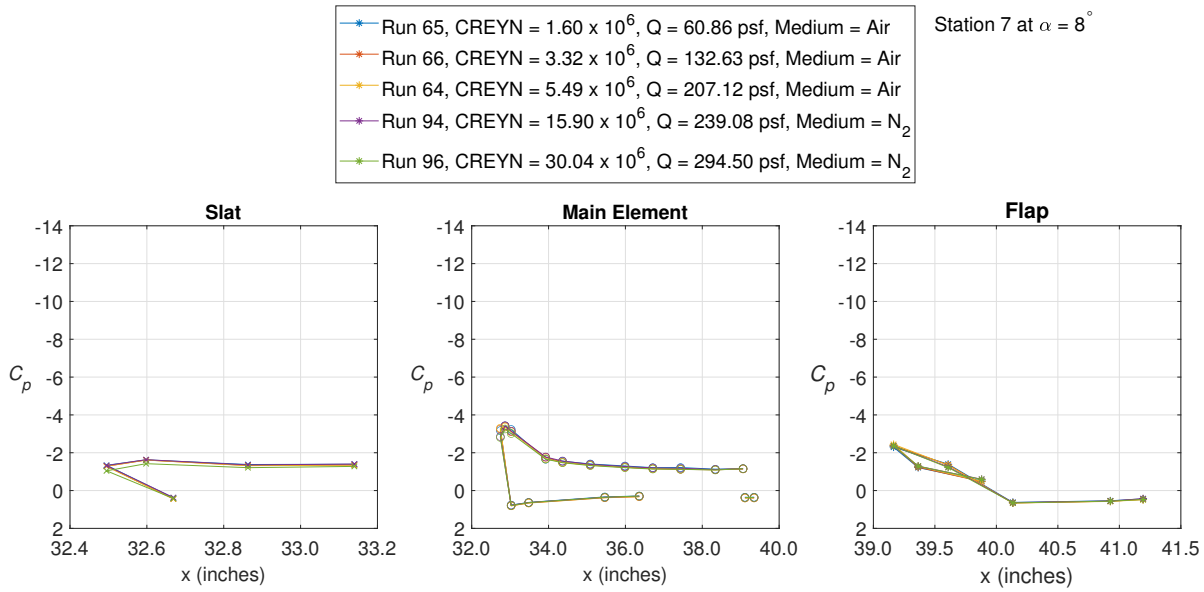


Fig. 28 Surface pressure coefficients at outboard wing station 7 in the landing configuration at varying chord Reynolds numbers at an angle of attack of $8°$, $M_\infty = 0.2$ (dimensions in model wing coordinate system, symbols indicate location: slat = x, main element = o, flap = *).

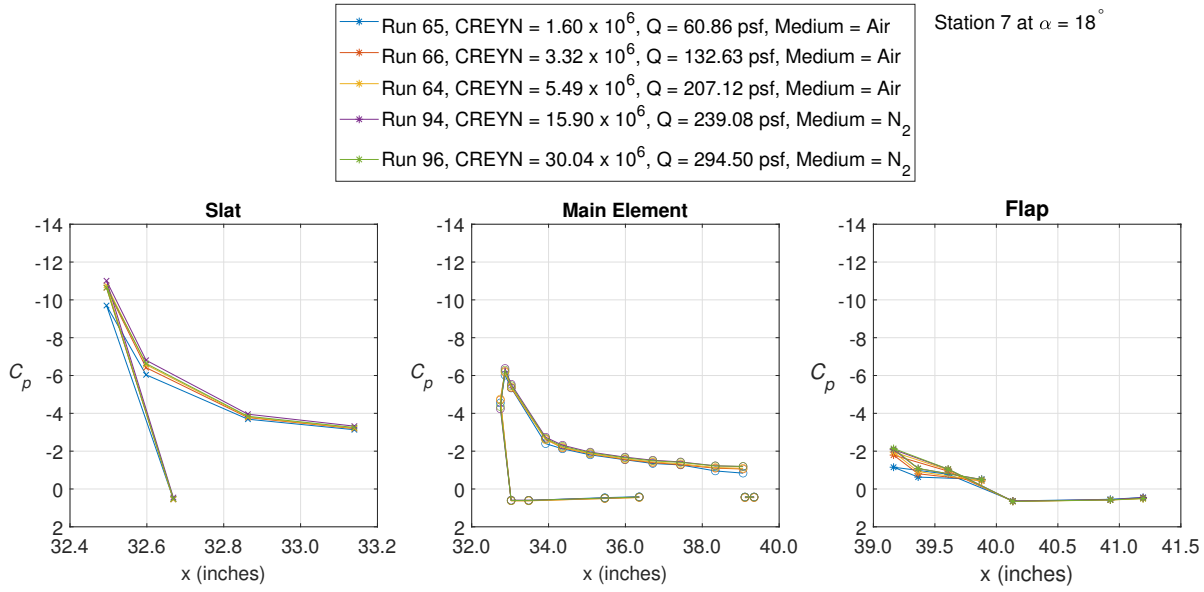


Fig. 29 Surface pressure coefficients at outboard wing station 7 in the landing configuration at varying chord Reynolds numbers at an angle of attack of $18°$, $M_\infty = 0.2$ (dimensions in model wing coordinate system, symbols indicate location: slat = x, main element = o, flap = *).

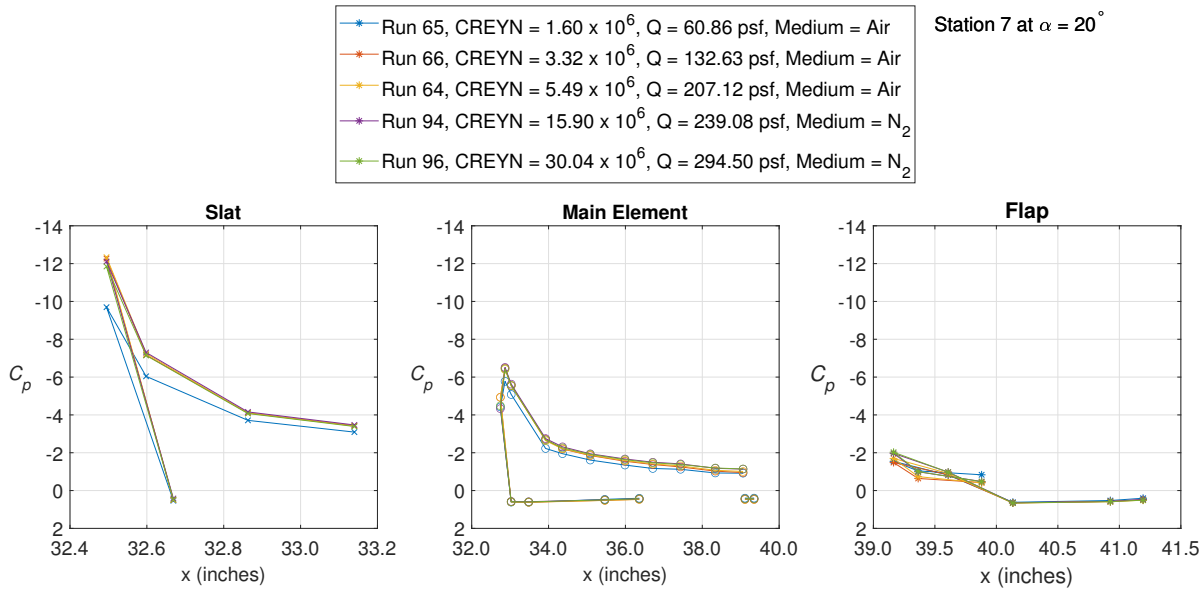


Fig. 30 Surface pressure coefficients at outboard wing station 7 in the landing configuration at varying chord Reynolds numbers at an angle of attack of $20°$**,** $M_\infty = 0.2$ **(dimensions in model wing coordinate system, symbols indicate location: slat = x, main element = o, flap = *).**

At all chord Reynolds numbers, for Stations 1 and 4, the slat and wing leading edge coefficient of pressure suction peaks increased (negatively) with increased angle of attack as the model approached $C_{L,max}$. Post stall, a slight reduction in the leading edge suction peaks was seen on the slat and wing. Relative to the flap, the leading edge coefficient of pressure suction peak reduced (positively) as angle of attack increased through post stall. For Station 7, the slat and the wing leading edge coefficient of pressure suction peaks increased (negatively) with increased angle of attack all the way through post stall. The flow on the flap may be separated for the entire angle of attack range shown, however, further investigation should be conducted. From these pressure plots, no conclusive Reynolds number trends could be drawn.

VI. Concluding Remarks

The 5.2%-scale CRM-HL model is a cryogenic-capable semispan model that was tested at chord Reynolds numbers from 1.6 million to 30 million in the NTF at LaRC. The model was heavily instrumented to collect force and moment and steady and unsteady pressure data. One of the primary test objectives was to determine the effect of Reynolds number on the force and moment behavior of the model. The initial data collected showed both expected and unexpected trends in the force and moment data. In general, the lift curves increased with increasing chord Reynolds number near $C_{L,max}$ and post stall, but not as much as expected from historical data of similar configurations. Overall, the lift increased and pitching moment decreased with increasing Reynolds number for chord Reynolds numbers less than 16 million. In the linear region of the lift curve, for chord Reynolds numbers below 16 million, the lift increased with increasing chord Reynolds numbers. The trend in the linear region of the lift curves at chord Reynolds numbers of 16 and 30 million did not follow the expected trends and merits further investigation. Surface pressure data were presented, but an aerodynamic phenomenon that would cause these anomalies in the force and moment data has yet to be identified. The low chord Reynolds number lift and drag curves compared well to prior testing of the 5.2%-scale CRM-HL model in atmospheric tunnels [5, 6]. Good agreement between overlapping chord Reynolds numbers (5.49 million) in both air and nitrogen modes at different dynamic pressures pointed toward an insensitivity of the model to aeroelastic effects for those specific chord Reynolds number conditions. However, at the higher chord Reynolds numbers, 16 and 30 million, there appeared to be some level of aeroelastic effects based on the trends in the data, but this should be further investigated. The effects of the nacelle, landing gear, and horizontal tail were isolated via configuration aerodynamics testing. The force and moment results of the component effects followed expected trends with some sensitivity to Reynolds number.

In the future, further investigation will be done using additional steady and unsteady pressure data and model deformation data taken during the test. A comparison will also be made when the TWICS data become available to determine if any trends change or any light is shed on the unusual behavior in the linear range of the lift curves

during select runs. Future testing is planned with the same model using flow visualization techniques such as particle tracking velocimetry to aid in identifying the flow physics and to better understand the aerodynamic phenomena occurring. Additional testing is also planned for a model at nearly half the scale (2.7%) in both a full-span and semispan configuration that will directly compare semi- to full-span effects.

Acknowledgments

The authors would like to thank and acknowledge the NTF staff for their hard work during a demanding test. The authors would also like to thank the NASA Transformational Tools and Technologies (TTT) Project of the Transformative Aeronautics Concepts Program and the Aerosciences Evaluation and Test Capabilities office both under the Aeronautics Research Mission Directorate for their funding and support of this work.

References

[1] "NASA Common Research Model," `https://commonresearchmodel.larc.nasa.gov/`, 2022. Accessed: 11 Nov 2024.

[2] Vassberg, J. C., et al., "Development of a Common Research Model for Applied CFD Validation Studies," *26th AIAA Applied Aerodyanmics Conference,* AIAA Paper 2008-6919, Honolulu, HI, 2008.

[3] Lacy, D. S., and Sclafani, A. J., "Development of the High Lift Common Research Model (HL-CRM): A Representative High Lift Configuration for Transonic Transports," *54th AIAA Aerospace Sciences Meeting,* AIAA Paper 2016-0308, San Diego, CA, 2016.

[4] Ertsgaard, M. L., and Winski, C. S., "Development of NASA 5.2%-Scale Semispan High Lift Common Research Model (CRM-HL)," *2025 AIAA SciTech Forum,* AIAA Paper 2025-XXXX, Orlando, FL, 2025. *To be published*.

[5] Winski, C. S., Langston, S. L., and Rivers, S. M., "NASA 5.2%-Scale Semispan High Lift Common Research Model Wind Tunnel Test at the 14- by 22-Foot Subsonic Wind Tunnel," *2025 AIAA SciTech Forum,* AIAA Paper 2025-XXXX, Orlando, FL, 2025. *To be published*.

[6] Puelm, S., Schmidt, F. N., Rudnik, R., and Winski, C. S., "Low-Speed Testing of the 5.2% Semi-Span CRM-HL in the DNW-NWB Wind Tunnel," *2024 AIAA Aviation Forum,* AIAA Paper 2024-3516, Las Vegas, NV, 2024.

[7] "National Transonic Facility (NTF) Overview," `https://www.nasa.gov/directorates/armd/aetc/national-transonic-facility-ntf/`, 2024. Accessed: 11 Nov 2024.

[8] NTF-Staff, "National Transonic Facility User Guide," *NASA Document SP-2012-12-354-LaRC*, 2012. NASA Langley Research Center.

[9] Lacy, D. S., and Clark, A. M., "Definition of Initial Landing and Takeoff Reference Configurations for the High Lift Common Research Model (CRM-HL)," *AIAA Aviation Forum 2020,* AIAA Paper 2020-2771, Virtual, 2020.

[10] Lynn, K., "Development of the NTF-117S Semi-Span Balance," *27th AIAA Aerodynamic Measurement Technology and Ground Testing Conference,* AIAA Paper 2010-4542, Chicago, IL, 2010.

[11] Walker, E. L., "Measuring Wall Interference Correction Accuracy: An Overview of the NTF Program," *42nd AIAA Aerospace Sciences Meeting,* AIAA Paper 2004-770, Reno, NV, 2004.

[12] Rivers, M. B., "Experimental Investigation of the NASA Common Research Model," *28th AIAA Applied Aerodynamics Converence,* AIAA Paper 2010-4218, Chicago, IL, 2010.

[13] Rivers, M. B., and Dittberner, A., "Experimental Investigation of the NASA Common Research Model in the NASA Langley National Transonic Facility and NASA Ames 11-Ft Transonic Wind Tunnel (Invited)," *49th AIAA Aerospace Sciences Meeting,* AIAA Paper 2011-1126, Orlando, FL, 2011.